Magnetotelluric multiscale 3-D inversion reveals crustal and upper mantle structure beneath the Hangai and Gobi-Altai region in Mongolia

J.S. Käufl[1], A.V. Grayver[1], M.J. Comeau[2], A.V. Kuvshinov[1], M. Becken[2], J. Kamm[2,3], E. Batmagnai[1], S. Demberel[4]

[1]*Institute of Geophysics, Department of Earth Sciences, ETH Zürich, Switzerland*

[2]*Institut für Geophysik, WWU Münster, Germany*

[3]*Geological Survey of Finland, Espoo, Finland*

[4]*Institute of Astronomy and Geophysics, Mongolian Academy of Sciences, Ulaanbaatar, Mongolia*

25 October 2019

Summary

Central Mongolia is a prominent region of intracontinental surface deformation and intraplate volcanism. To study these processes, which are poorly understood, we collected magnetotelluric data in the Hangai and Gobi-Altai region in central Mongolia and derived the first three-dimensional (3-D) resistivity model of the crustal and upper mantle structure in this region.

The geological and tectonic history of this region is complex, resulting in features over a wide range of spatial scales, which that are coupled through a variety of geodynamic processes. Many Earth properties that are critical for the understanding of these processes, such as temperature as well as fluid and melt properties, affect the electrical conductivity in the subsurface. 3-D imaging using magnetotellurics can resolve the distribution of electrical

conductivity within the Earth at scales ranging from tens of metres to hundreds of kilometres, thereby providing constraints on possible geodynamic scenarios. We present an approach to survey design, data acquisition, and inversion that aims to bridge various spatial scales while keeping the required field work and computational cost of the subsequent 3-D inversion feasible.

Magnetotelluric transfer functions were estimated for a 650×400 km^2 grid, which included measurements on an array with regular 50×50 km^2 spacing and along several profiles with a denser 5-15 km spacing. The use of telluric-only data loggers on these profiles allowed for an efficient data acquisition with a high spatial resolution. A 3-D finite element forward modelling and inversion code was used to obtain the resistivity model. Locally refined unstructured hexahedral meshes allow for a multi-scale model parametrization and accurate topography representation. The inversion process was carried out over four stages, whereby the result from each stage was used as input for the following stage that included a finer model parametrization and/or additional data (i.e. more stations, wider frequency range).

The final model reveals a detailed resistivity structure and fits the observed data well, across all periods and site locations, offering new insights into the subsurface structure of central Mongolia. A prominent feature is a large low-resistivity zone detected in the upper mantle. This feature suggests a non-uniform lithosphere-asthenosphere boundary that contains localized upwellings that shallow to a depth of 70 km, consistent with previous studies. The 3-D model reveals the complex geometry of the feature, which appears rooted below the Eastern Hangai Dome with a second smaller feature slightly south of the Hangai Dome.

Within the highly resistive upper crust, several conductive anomalies are observed. These may be explained by late Cenozoic volcanic zones and modern geothermal areas, which appear linked to mantle structures, as well as by major fault systems, which mark terrane boundaries and mineralized zones. Well resolved, heterogeneous low-resistivity zones that permeate the lower crust may be explained by fluid-rich domains.

1 INTRODUCTION

Located deep in the continental interior, far away from plate boundaries, central Mongolia is a region of active intracontinental deformation (Calais et al. 2003; Walker et al. 2007, 2008) and young Cenozoic volcanism (e.g. Barry et al. 2003; Ancuta et al. 2018). With the stable Siberian Craton to the North, central Mongolia occupies the transition zone between the North-South compressional regime of the India-Asia collision and an eastward motion (Calais et al. 2003). This transition zone is dominated by the Hangai Dome, a low relief, intracontinental plateau elevated up to 2 km above the regional average (Cunningham 2001). It is bounded by large seismically active strike slip faults, which experienced large (Magnitude > 8, Rizza et al. 2015) intracontinental earthquakes in the last century (Walker et al. 2007). Additionally, dispersed, low-volume, intraplate volcanism has occurred during the last 35 Ma throughout central Mongolia (Barry et al. 2003; Hunt et al. 2012; Ancuta et al. 2018).

The cause of the volcanism and the mechanism for the Hangai Dome uplift remain enigmatic. In particular, the link between intracontinental uplift and intraplate volcanism is an open topic of research. In the case of central Mongolia, some authors argue for contemporaneous processes (e.g. Cunningham 2001; Sahagian et al. 2016), whereas others suggest that the uplift might have predated the volcanic activity (McDannell et al. 2018).

Previous seismic and gravity studies of the region found a low velocity/low density anomaly in the upper mantle below the Hangai Dome confined to depths of $70 - 150$ km (Priestley et al. 2006; Tiberi et al. 2008), and a low shear-wave velocity anomaly that possibly extends to a depth of more than 410 km (Chen et al. 2015). Across central Mongolia, a thick crust (45–55 km) was determined by seismic studies, with the thickest part directly below the Hangai Dome (Petit et al. 2008). Seismic studies also observed a shallow (60–80 km) lithosphere-asthenosphere-boundary (LAB) below the Hangai Dome (Priestley et al. 2006;

Petit et al. 2008). Geochemical analysis of erupted lavas and mantle xenoliths estimates the melting source at depths of 70 to 150 km (Ionov 2002; Barry et al. 2003; Hunt et al. 2012), in good agreement with a shallow asthenosphere and with the observed low velocity/low density anomalies.

This combined evidence is inconsistent with an earlier explanation for the intraplate volcanism: a deep-rooted mantle plume (Windley & Allen 1993). More recent explanations for the volcanism and uplift include crust-mantle interactions such as lithospheric thinning (due to delamination, convective removal, or edge-driven convection) or asthenospheric flow and dynamic topography (see e.g. Ancuta et al. 2018). However, a comprehensive explanation is still missing, partly due to a lack of detailed images of the subsurface in this region. To obtain this information, a magnetotelluric survey was conducted in the Hangai and Gobi-Altai region from 2016 to 2018.

Magnetotellurics (MT) images the electrical resistivity of the subsurface, which is primarily controlled by the quantity and composition of fluids, the porosity, and the temperature (e.g. Unsworth & Rondenay 2013; Manning 2018). Low-resistive domains in the crust or upper mantle can therefore often be associated with the presence of inter-connected saline fluids or partial melts. Because fluid (and melt) networks lower the bulk resistivity and can have a mechanical weakening effect on rocks (Liu & Hasterok 2016), resistivity images allow for inferences on the rheology of the lithosphere. Comprehensive geodynamic scenarios should therefore ultimately be able to account for resistivity images from MT.

In the past, three-dimensional (3-D) inversion of MT data has been used to successfully image the subsurface from the crust into the upper mantle. On a local scale, MT provided models of shallow volcanic and geothermal systems with small extents of approximately 10 km (e.g. Heise et al. 2007; Bertrand et al. 2012; Muñoz 2014; Hill et al. 2015; Peacock et al. 2016; Usui et al. 2016; Samrock et al. 2018). At regional scales, MT is commonly used to image crustal and lithospheric structures (e.g. Khoza et al. 2013; Tietze & Ritter 2013; Nieuwenhuis et al. 2014; Cherevatova et al. 2015; Robertson et al. 2017; Xu et al. 2019) and in recent years, models obtained by inverting continental scale surveys have appeared,

including the USArray, AusLAMP, and SinoProbe projects (e.g. Meqbel et al. 2014; Yang et al. 2015; Robertson et al. 2016; Dong et al. 2016; Murphy & Egbert 2017). However, the resistivity anomalies related to geological and geodynamic processes caused by crust-mantle interactions, such as the intracontinental deformation and intraplate volcanism in Mongolia, can be observed over the entire range of spatial scales covered in these surveys. Hence, this was the motivation to design a MT survey and develop a 3-D inversion scheme that can consistently embrace and bridge multiple spatial scales.

In practice, any survey design is often limited by the cost of data acquisition and the required logistical effort. Because a uniform, dense grid of sites can be prohibitively expensive to collect, an attractive alternative is complementing a coarser, large-scale grid of sites with more densely spaced sites in regions of primary interest. Data acquisition can further be optimized with the Telluric-Magnetotelluric (T-MT) method (Hermance & Thayer 1975), whereby the magnetic field is recorded only at a subset of locations (Iliceto & Santarato 1986; Yungul 1977; García & Jones 2005; Melosh et al. 2010; Campanyà et al. 2014). From a methodological perspective, handling T-MT data requires only modest modifications to the data processing and inversion tools to take full advantage of simultaneously recording arrays (Egbert 2002). For the three-dimensional interpretation of MT data collected at an observation grid of highly variable spacing, one needs an inversion strategy that provides sufficient flexibility in parametrizing the subsurface. This allows varying lateral and vertical resolution lengths to be appropriately accounted for without using an excessive number of unknown model parameters, which would impose additional computational constraints and increase non-uniqueness.

In this paper we focus on the methodological side of the problem and present an approach on how to bridge the different spatial scales in 3-D MT inversions, applied to the data collected in the Hangai and Gobi-Altai mountains in central Mongolia. Conductive anomalies are described, and potential explanations, in the context of the regional geodynamics and geology, are offered. Earlier results by Comeau et al. (2018c), based on a 2-D model from a subset of the data, are expanded upon with new insights from the 3-D resistivity model.

2   DATA

2.1   The magnetotelluric method

The MT method is a geophysical technique used to probe the conductivity structure of the Earth by using natural electromagnetic (EM) field variations (Rikitake 1948; Tikhonov 1950; Cagniard 1953). The Earth's response to external excitation is described by frequency-dependent transfer functions (TF), which carry information about the electrical conductivity distribution. We work with the magnetotelluric impedance tensor $\mathbf{Z}$, which links horizontal electric and magnetic fields as:

$$\vec{E}_h(\omega, \vec{r}_l) = \mathbf{Z}(\omega, \vec{r}_l)\,\vec{H}_h(\omega, \vec{r}_l). \tag{1}$$

Here, ω is the angular frequency. $\vec{E}_h(\omega, \vec{r}_l) = (E_x, E_y)$ and $\vec{H}_h(\omega, \vec{r}_l) = (H_x, H_y)$ are the Fourier transforms of the horizontal components of the electric (E-) and magnetic (H-) fields at the location $\vec{r}_l$. Henceforth, the frequency dependence is implied and will be omitted for simplicity. H- and E-fields act as the input and output of the linear system described by the impedance

$$\mathbf{Z}(\vec{r}_l) = \begin{pmatrix} Z_{xx}(\vec{r}_l) & Z_{xy}(\vec{r}_l) \\ Z_{yx}(\vec{r}_l) & Z_{yy}(\vec{r}_l) \end{pmatrix}, \tag{2}$$

which is a second-order frequency dependent, complex-valued tensor. It carries the information about the 3-D electrical conductivity distribution σ in the earth. Instead of the conductivity, its inverse, the resistivity ($\rho = \sigma^{-1}$) can be used interchangeably. For each of the four tensor elements we can calculate the phase

$$\phi_{ij}(\vec{r}_l) = \tan^{-1}(Z_{ij}(\vec{r}_l)) \qquad \text{with} \quad i, j \in \{x, y\} \tag{3}$$

and apparent resistivity

$$\rho_{a,ij}(\vec{r}_l) = \frac{|Z_{ij}(\vec{r}_l)|^2}{\omega\mu_0}, \tag{4}$$

where μ_0 is the magnetic permeability of vacuum.

Conventionally, electric and magnetic fields are recorded at the same location $\vec{r}_l$. The T-MT method (Hermance & Thayer 1975) introduces an inter-site impedance, $\mathbf{Z}_i$, defined

148 as

$$\vec{E}_h(\vec{r}_l) = \mathbf{Z}_i(\vec{r}_l, \vec{r}_b)\,\vec{H}_h(\vec{r}_b), \qquad (5)$$

149 whereby $\mathbf{Z}_i$ is calculated with the E-field measured at the location $\vec{r}_l$ and the H-field mea-

150 sured at the location $\vec{r}_b$ (denoted as base site). The different locations of E-field and B-field

151 measurements ($\vec{r}_l$ and $\vec{r}_b$) are taken into account for the forward modelling and inversion

152 of intersite impedances (see Sections 3.1 and 3.2 below). Recently, Comeau et al. (2018c)

153 inverted a single profile of MT data across Mongolia and showed that using $\mathbf{Z}_i$ does not

154 compromise resolution and leads to reliable subsurface images. In fact, this approach can

155 further help in suppressing local noise (Egbert 2002; Campanyà et al. 2014).

156 2.2   Data acquisition

157 During three field surveys in the years 2016 to 2018, data was collected on a 650×400 km^2

158 grid (see Fig. 1 and Table 1 for abbreviations of geographic features). The survey covers

159 the Hangai Mountains, a part of the Gobi-Altai mountain range, the Valley of Lakes, and

160 surrounding areas. For the inversion model presented below, we use transfer functions from

161 272 unique locations with 97 sites laid out on a quasi-uniform grid with 50 km spacing and

162 175 sites along four profiles (P2, P3, P4, and P6 in Fig. 1) with a spacing of 5 to 15 km.

163 Additional sites are located in the Tariat volcanic field (TV, Comeau et al. 2018a) and the

164 Tsenkher geothermal area (TGT).

165   We employed two types of instruments: broadband (B) and telluric-only (T). Generally,

166 B-instruments were used for the grid sites, while T-instruments were installed on the pro-

167 files. For some of the sites we had to deviate from this scheme due to data quality issues

168 and instrument availability during the measurement campaign. All instruments recorded

169 the horizontal electric field (60 m dipole length with either silver-chloride or lead-chloride

170 electrodes). B-sites additionally recorded all three components of the magnetic field. At B-

171 locations, Metronix ADU-07e and SPAM Mk4 data loggers with Metronix induction coils

172 (MFS-06 and MFS-10) were used. Recording was done for three to five days with a sampling

173 frequency of 512 Hz. Additional long period instruments (Geomag Fluxgate and EarthData
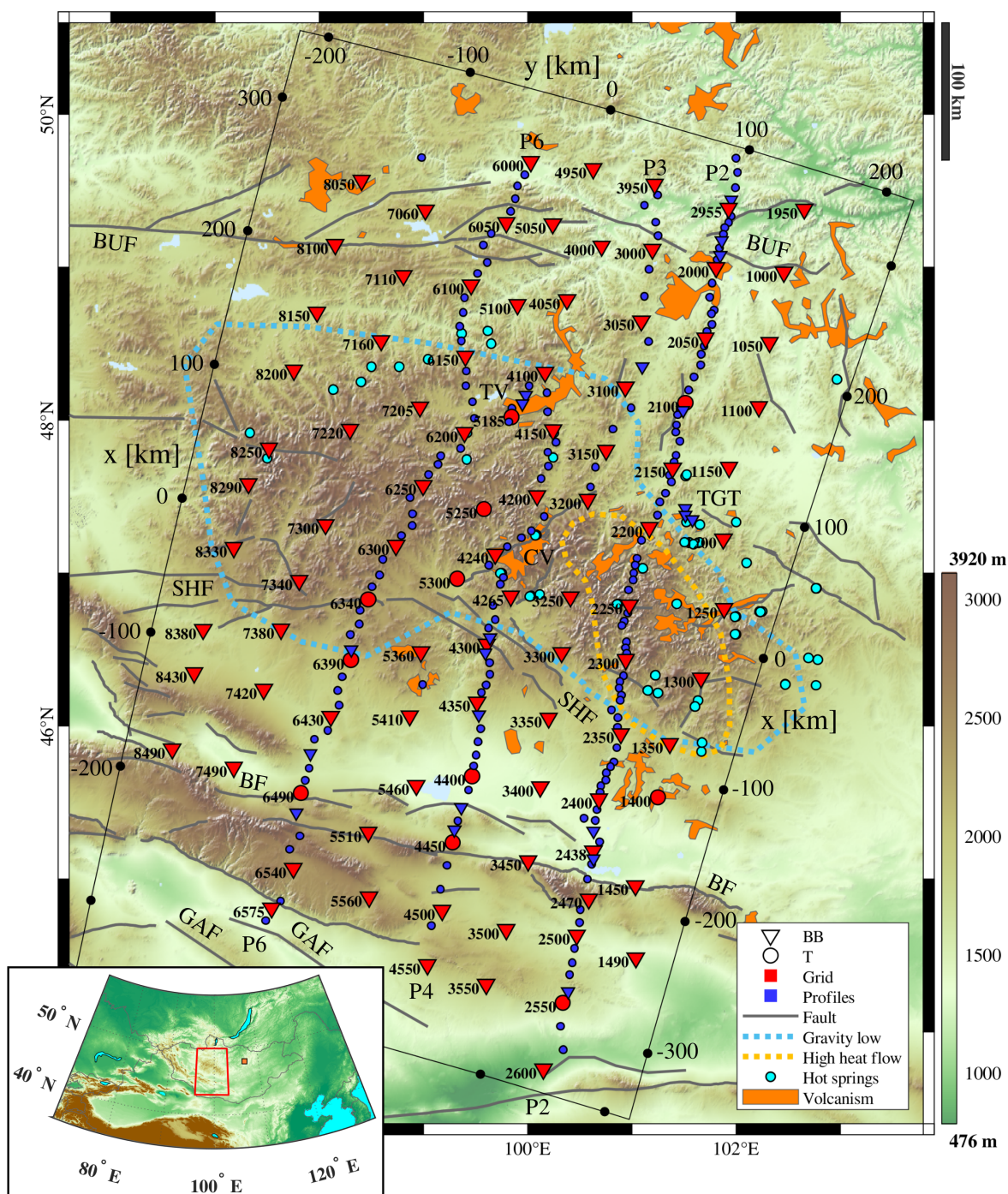
Figure 1. Topographic map with installed sites in central Mongolia. The location in central Asia is indicated in the smaller inset in the lower left. See Table 1 for abbreviations. The symbol indicates the type of instrument used. Red color indicates the grid sites and blue color the others. The grid sites are indicated with their numeric designation. Grey lines mark major fault systems (Walker et al. 2008; Styron 2018), the dotted blue line indicates the -250 mGal Bouguer anomaly (Tiberi et al. 2008), the dotted orange line indicates the 90 mW/m² high heat flow anomaly, light blue circles mark hot spring locations (Oyuntsetseg et al. 2015; Ganbat & Demberel 2010), and the orange patches designate Cenozoic volcanic provinces (Ancuta et al. 2018). The black frame around the survey area indicates the rotated local cartesian coordinate system used for the 3-D inversion.

AS:	Asthenosphere
BF:	Bogd fault
BUF:	Bulnay fault
CV:	Chuluut volcanic zone
EHC:	East Hangai conductor
GAC	Gobi-Altai conductor
GAF:	Gobi-Altai fault
HB:	Hangai block
LAB:	Lithosphere-Asthenosphere boundary
NHC:	North Hangai conductor
SHC:	South Hangai conductor
SHF:	South Hangai fault
TV:	Tariat volcanic zone
TGT:	Tsenkher geothermal area
VL:	Valley of Lakes
VLR:	Valley of Lakes resistor
WHC:	West Hangai conductor

Table 1. Table of abbreviations used throughout the text and in figures.

data loggers) were installed at 14 locations along profiles P2 and P4. Recording time was between 10 and 32 days with a sampling frequency of 2 Hz. The telluric instruments were designed by the University of Münster for fast and easy deployment, thus allowing for efficient data collection with dense site spacing. They recorded with a sampling frequency of 512 Hz for a duration of twelve hours to three days.

2.3 Transfer functions

Impedance tensors were estimated with a robust processing scheme, using the M-estimator (Egbert & Booker 1986) and a minimal covariance determinant method (Rousseeuw 1984; Platz & Weckmann 2019) to improve long period TF when only a few time windows are available (Harpering 2018). To maximise the quality and period range of TF, processing parameters (such as time window selection, bi-coherence threshold values, single site or remote referencing, base site selection for inter-site impedances) were chosen individually
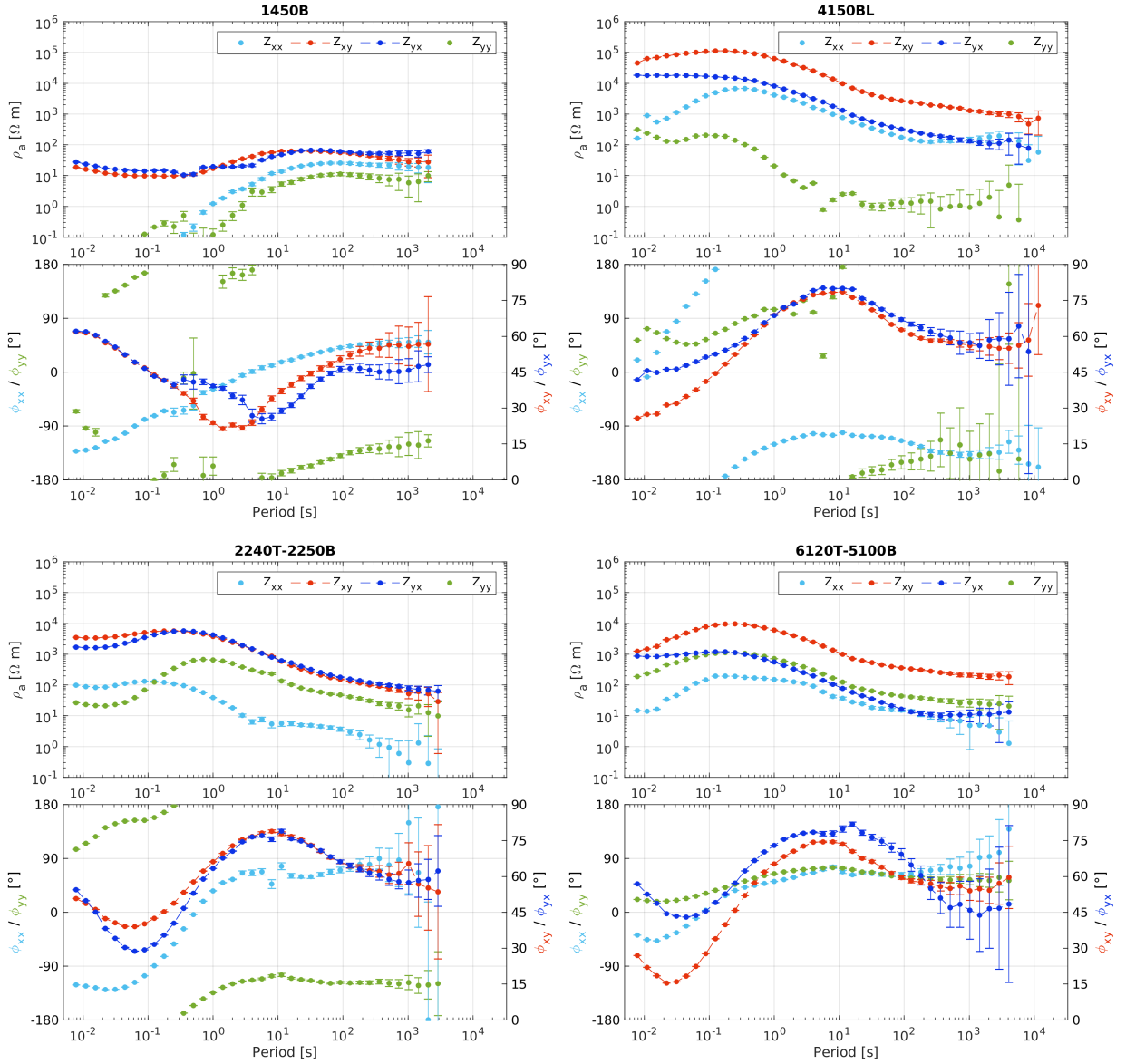
Figure 2. Apparent resistivity and phase curves at four representative sites. The off-diagonal phases (ϕ_{xy} and ϕ_{yx}) are shifted to the first quadrant for better visibility. 1450B is a broadband site, 4150BL is a broadband and long-period site, 2240T and 6120T are telluric sites with their respective base sites given in the plot titles.

for each site. After processing, we obtained a set of 272 TF of high quality in the period range from 0.0078 s to 3000 s at most sites with periods going up to 8000 s and 24000 s for some broad-band and long-period sites, respectively. Fig. 2 shows a representative set of transfer functions at four locations.

Overall, the data is affected by galvanic distortions. For instance, 4150BL in Fig. 2

191 exhibits a static shift effect for $T > 0.5$ s (large differences between ρ_{xy} and ρ_{yx} but with

192 similarly-shaped curves, as well as similar ϕ_{xy} and ϕ_{yx}). Berdichevsky et al. (1980) suggested

193 that an regional 1-D impedance can be obtained with the geometric mean of the determinant

194 of **Z**. In this paper, we use the sum of the squared impedance elements (SSQ-impedance)

$$Z_{ssq}(\vec{r}_l) = \sqrt{\frac{Z_{xx}(\vec{r}_l)^2 + Z_{xy}(\vec{r}_l)^2 + Z_{yx}(\vec{r}_l)^2 + Z_{yy}(\vec{r}_l)^2}{2}} \tag{6}$$

195 for each location $\vec{r}_l$. Compared to the impedance determinant, Z_{ssq} is less affected by a

196 downward bias due to distortion (Rung-Arunwan et al. 2016). The regional 1-D impedance,

$$\bar{Z}_{\text{1-D}} = \sqrt[N]{\prod_{l=1}^{N} Z_{ssq}(\vec{r}_l)}, \tag{7}$$

197 is calculated with the geometric average, where N denotes the total count of locations used.

198   The apparent resistivities and phases obtained from the SSQ-impedances for the grid sites

199 north and south of the South Hangai Fault (SHF) are shown in Fig. 3a) for periods $T > 1$ s.

200 Generally, we see in Fig. 3a) that Z_{ssq} from northern sites (see e.g. 4150BL, 2240T, and 6120T

201 in Fig. 2) exhibit much less spatial variability compared to the sites south of the SHF (see e.g.

202 1450B in Fig. 2 as well as 2350BL and 4350BL in Fig. 5). Apparent resistivities for northern

203 sites vary over two orders of magnitude, most likely due to galvanic distortions, but the shape

204 of the ρ_a curves and the phase shows smaller variability, especially for periods $T > 10$ s.

205 We conclude that the 1-D impedance calculated from averaged northern SSQ-impedances

206 provides a reasonable representation of the regional 1-D conductivity structure. Southern

207 sites, on the other hand, show a large variability in both ρ_a and ϕ curves over the entire

208 period range, indicating a substantially inhomogeneous regional conductivity distribution.

209 As a result, the southern regional 1-D impedance is likely not representative of a regional

210 conductivity structure.

211   Further, Fig. 3b shows the real part of the C-response,

$$C = -\frac{\bar{Z}_{\text{1-D}}}{i\omega\mu_0}, \tag{8}$$

212 calculated for both regional 1-D impedances. It represents the depth of the "center of mass"

213 of induced currents for a given period (Weidelt 1972) and can be used as a proxy for the
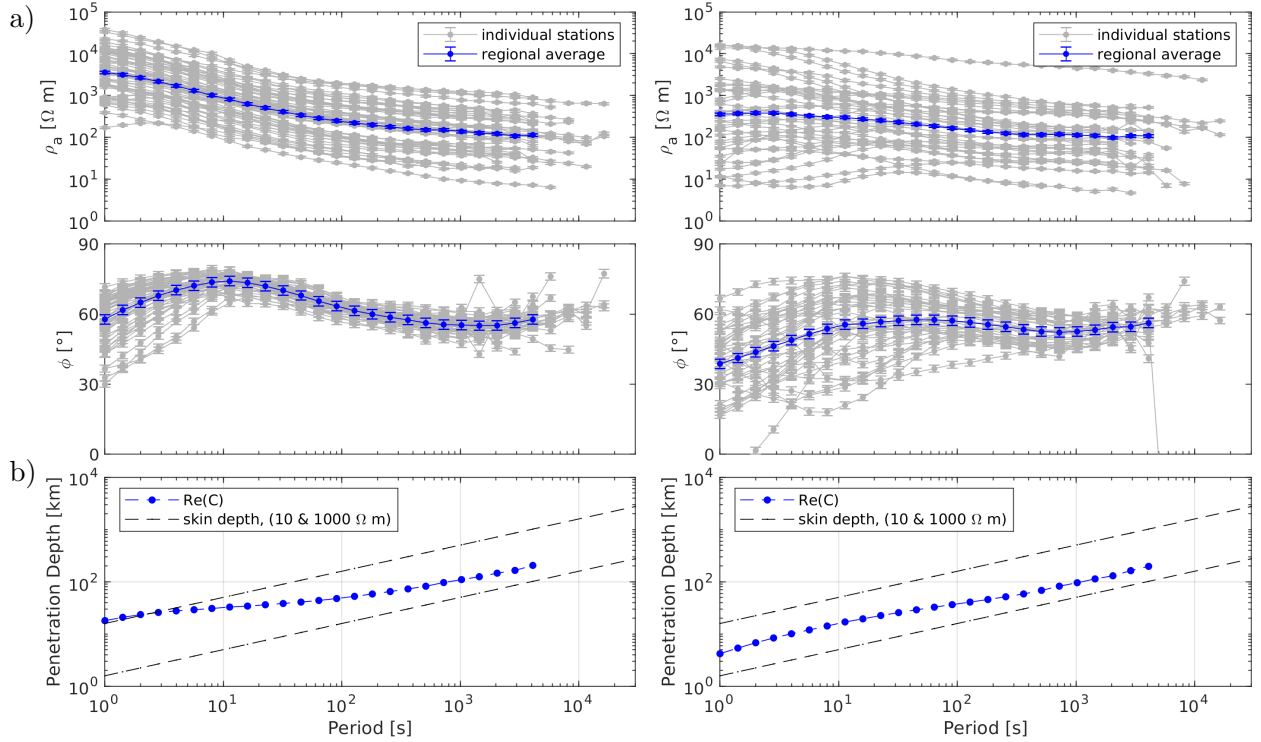
Figure 3. SSQ-impedances and penetration depths estimated from grid site data north (left) and south (right) of the SHF (see Fig. 1). a) ρ_a and ϕ calculated from the SSQ-impedance of each individual site (grey) and from the regional 1-D impedance (Eq. 7; blue). b) The real part of the C-response for both regional 1-D averages, a measure for the penetration depth, together with the skin depths for a homogeneous half space of 10 and 1000 Ωm.

penetration depth. Starting with a penetration depth of 4-15 km at 1 s, the penetration depth increases to 200 km at the period of 4096 s.

We performed a dimensionality analysis by calculating the phase tensor strike angle θ and the normalized skew angle Ψ (Booker 2014). The polar histograms of θ in Fig. 4 reveals a preferred strike direction for periods $T > 10$ s, namely $15° \pm 90°$ (clockwise from magnetic North). With a normalized skew angle of $|\Psi| > 6°$ over a wide period range at the majority of the sites (see the supplementary material, Sec. S1), the collected data shows a significant influence of 3-D effects (Booker 2014). Thus a 3-D inversion is indeed indispensable to retrieve all information from the dataset.

As was previously shown by Tietze & Ritter (2013), when a predominant geological strike direction exists, it is advantageous to rotate the impedance tensor even for 3-D inversion,
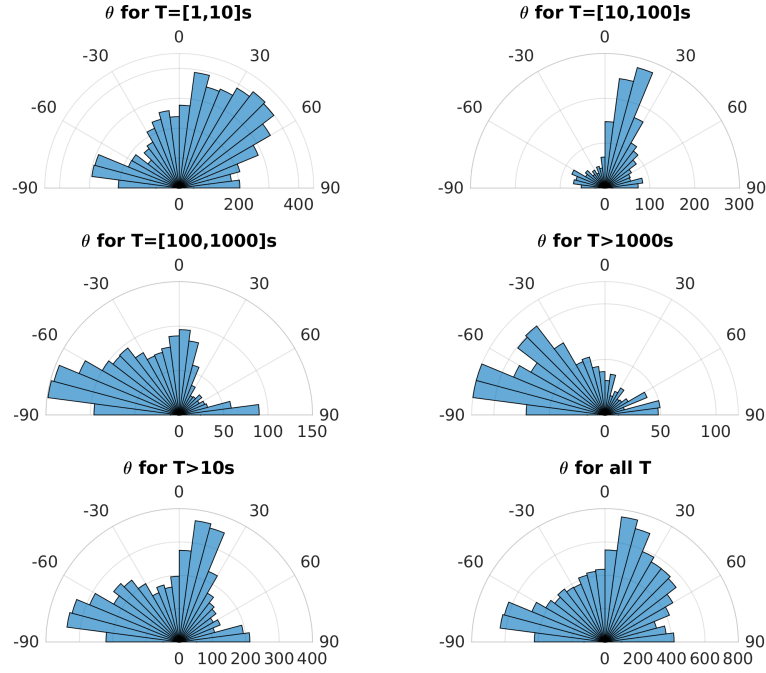
Figure 4. Polar histograms of the phase tensor strike angle θ (clockwise from magnetic North) for different period bands. From 10 s to 100 s a clear strike direction of 15° can be seen, whereas longer periods show a strike of -75°.

thereby improving inversion convergence and reducing modelling errors. Therefore, we rotated the impedance tensors by 15° counter-clockwise, thus aligning the principal axes not only with the strike directions but also the profile directions. An additional benefit of the rotation is the correction of out of quadrant off-diagonal phases, that can be observed at some of the sites. This is shown in Fig. 5 for two sites, 2350BL and 4350BL. For both sites $\rho_{xy} > \rho_{yx}$, indicating East-West oriented low resistivity anomalies. A phase tensor analysis of these sites reveals strong 3-D influences with a normalized skew angle of $|\Psi| > 6°$ in the period range of 0.1–10 s, indicating that shallow (less than 10 km) 3-D anomalies are most likely the cause of these out of quadrant phases. After rotating the impedance tensor by 15° counter-clockwise from magnetic North, phases remain in their respective quadrants for the entire period range.
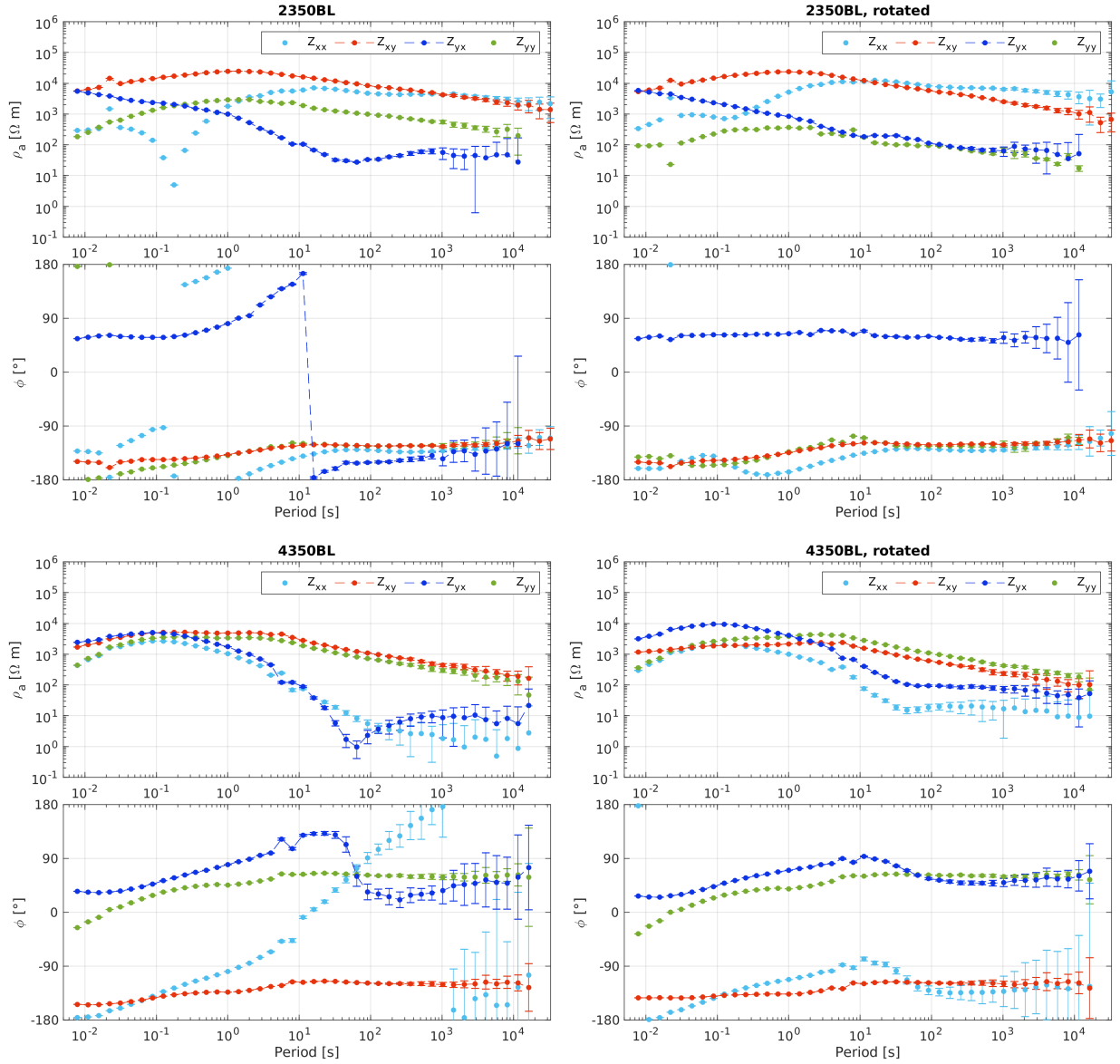
Figure 5. Sounding curves for the sites 4350BL and 2350BL, left: coordinate system oriented along magnetic North, right: rotated coordinate system (15° counterclockwise from magnetic North). After rotation, previously out of quadrant phases remain in their respective quadrants over the entire period range.

3   METHODOLOGY

Owing to the wide frequency range of MT source signals (10^{-4} to $\approx 10^5$ s), together with the typical electrical resistivity range of the Earth (0.1 to 10^5 Ωm), the inversion of MT data can efficiently resolve electrical resistivity variations in a wide range of spatial scales from tens of metres to hundreds of kilometres. Here, we aim at combining MT data from

a regional-scale array and locally dense profile sites, encompassing a period range over five decades. We address this challenge by introducing a 3-D multi-scale inversion scheme. Our approach is outlined below.

3.1 Forward modelling

Electromagnetic fields in a 3-D medium are calculated by solving the following equation

$$\nabla \times (\mu_0^{-1} \nabla \times \vec{E}) + i\omega\sigma\vec{E} = 0 \qquad \text{in} \quad \Omega. \tag{9}$$

Here, $\Omega \subseteq R^3$ is the modelling domain, $\vec{E}$ the electric field vector and σ the electrical conductivity. Further, the inhomogeneous Dirichlet boundary conditions,

$$\vec{E} = \vec{E}_0 \quad \text{on} \quad \partial\Omega, \tag{10}$$

are applied, where $\vec{E}_0$ results from the solution of 2-D Maxwell's equations on the boundaries. The magnetic field $\vec{H}$ is obtained by virtue of Faraday's law. Solutions for two orthogonal source polarisations are computed to be able to derive the full impedance tensor.

The 3-D finite element code GoFEM (Grayver & Kolev 2015) was used to discretize Eq. (9) and find a numerical solution. It is based on the finite-element library deal.II (Alzetta et al. 2018) and uses PETSc (Balay et al. 2018) with METIS (Karypis & Kumar 1999) for distributed linear algebra and mesh partitioning, respectively. The resulting system of linear equations was solved with a parallel version of the iterative FGMRES solver and auxiliary-space multigrid preconditioner as described in detail by Grayver & Kolev (2015). To improve accuracy of the numerical solutions and to discretize topography accurately, we used locally refined non-conforming hexahedral meshes, as described in Section 3.3.

3.2 Inversion

To obtain the electrical conductivity distribution that explains the measured data we solve a non-linear inverse problem (e.g. Dmitriev et al. 1976; Aster et al. 2018) by minimising the objective function

$$\Phi(\mathbf{m}) = \frac{1}{2}\Phi_d(\mathbf{d}, \mathbf{m}) + \frac{\alpha}{2}\Phi_m(\mathbf{m}), \tag{11}$$

which consists of a data term Φ_d and a model term Φ_m, balanced by the regularization parameter α. $\mathbf{m}$ is a vector of the unknown model parameters (i.e. the electrical conductivity) and $\mathbf{d}$ the data vector, containing the TF. For this study we used the real and imaginary parts of either the regional 1-D impedance (Eq. 7, for a 1-D inversion) or all four impedance tensor components (Eq. 2, for a 3-D inversion). Given that the phase tensors indicate strong 3-D effects in parts of the data, 2-D/3-D tensor decompositions (e.g. Groom & Bailey 1989; Bahr 1991; Smith 1997) are not applicable. Therefore, no attempt was made to correct for galvanic distortion.

The data term

$$\Phi_d(\mathbf{m}, \mathbf{d}) = ||(f(\mathbf{m}) - \mathbf{d})||^2_{\mathbf{C}_d^{-1}} \, , \tag{12}$$

contains the difference between the observed and the modelled TFs, which are obtained from the forward modelling operator $f(\mathbf{m})$ given a model $\mathbf{m}$. The data is weighted by the the data covariances $\mathbf{C}_d$, given here by a diagonal matrix containing the data variance δZ^2.

Because of strong galvanic distortions, a relative error e was applied row-wise to the absolute of $\mathbf{Z}$ at each period, giving data variances

$$\delta Z^2_{jx} = \delta Z^2_{jy} = (e \cdot \max(|Z_{jx}|, |Z_{jy}|))^2 \qquad \text{with} \quad j \in \{x, y\}. \tag{13}$$

To prevent imbalance between grid and profile sites, we found that an error $e = 0.03$ for the grid and $e = 0.05$ for the profiles allows us to achieve a uniform fit for all sites. Thereby, TF at the profile sites are slightly down-weighted in comparison to TF from the grid sites.

The model or regularization term

$$\Phi_m(\mathbf{m}) = ||R(\mathbf{m})||^2 \tag{14}$$

is given by the roughness operator $R(\vec{m})$, aimed to stabilize the ill-posed and generally non-unique inverse problem (Tikhonov 1963). No reference model is used in the regularization term. Thereby, the roughness of the model (characterized by the conductivity jumps across adjacent cells) is minimized.

GoFEM uses the Gauss-Newton method to minimize the functional in Eq. (11) (Grayver

2015). A unit step length for the model update is used. While this can lead to an increase in Φ, it usually allows the inversion to escape a local minimum.

The regularization parameter

$$\alpha = \gamma \frac{||\mathbf{J}^T \mathbf{C}_d^{-1} \mathbf{J}||_2}{||\mathbf{R}||_2} \tag{15}$$

is determined for each iteration step by the ratio of the L_2-norms of the weighted approximate Hessian $\mathbf{J}^T \mathbf{C}_d^{-1} \mathbf{J}$ and the regularization matrix $\mathbf{R}$. $\mathbf{J}$ denotes the Jacobian of $f(\mathbf{m})$. The scaling factor $\gamma \in (0, 1]$ is a user-determined parameter. We adopted a cooling regularization by gradually decreasing the regularization strength through smaller γ. In practice, this approach facilitates the recovery of the dominating large-scale conductivity variations followed by smaller structures later during the inversion process.

3.3   Model discretization

The modelling domain Ω is discretized using hexahedral elements. To ensure numerical accuracy and to decrease the ambiguity of the non-unique problem, we use locally refined meshes. As outlined by Käufl et al. (2018), an initially coarse mesh is locally refined within the area of interest and then transformed to conform to the topography.

The mesh used in this study has a size of $4000 \times 4000 \times 3000$ km^3 and consists of 6800 cells initially. The subsequent refinements were guided by the penetration depth inferred from the C-responses (Fig. 3b). After two refinements at the air-ground interface, three refinements in the central area of interest, and three refinements around site locations, the mesh consists of 215000 cells. Within the survey area, cell diameters range from 4.7 km close to the MT sites to 19 km in the upper mantle down to a depth of 200 km. At greater depths and outside the survey area, cells increase gradually towards the domain boundary. Finally, the meshes are adjusted to the topography (elevation data provided by NASA JPL 2013) and cells in the air are assigned a resistivity of 10^9 Ωm. The resulting mesh is shown in Fig. 6a. A second finer mesh is obtained by further refinement, resulting in 321000 cells with a minimal cell diameter of 2.4 km near sites (Fig. 6b). This represents our inverse model parametrization.

³¹¹ As is shown by Joshi et al. (2004) and Grayver (2015), it may be advantageous to decou-

³¹² ple forward/adjoint and inverse model parametrizations. Specifically, we use an additional

³¹³ refinement step in a 5 km radius around site locations for forward and adjoint solutions in

³¹⁴ order to better represent local topography and increase numerical accuracy for higher fre-

³¹⁵ quencies. A coarser mesh for the targeted parameter (that is, electrical conductivity) reduces

³¹⁶ computational cost and decrease ambiguity, thereby making the problem less ill-posed. Note

³¹⁷ that due to hierarchical relation between both forward/adjoint and inverse grids, we avoid

³¹⁸ any interpolation and simply assign conductivity from the coarser inverse grid cells to refined

³¹⁹ forward/adjoint grid cells.

³²⁰ Following the arguments from Section 2.3, we perform the inversion in a local Cartesian

³²¹ coordinate system with x- and y-axes rotated 15° clockwise from North and East respectively.

³²² The z-axis points downward. The origin corresponds to the center of the survey grid at

³²³ 47°N, 99.5°E (sea level). All geographic coordinates are transformed into the modelling

³²⁴ domain by referencing their UTM coordinates (zone 47, WGS84 reference ellipsoid) to 47°N,

³²⁵ 99.5°E followed by a rotation around the origin. The resulting cartesian coordinate system

³²⁶ is indicated in Fig. 1.
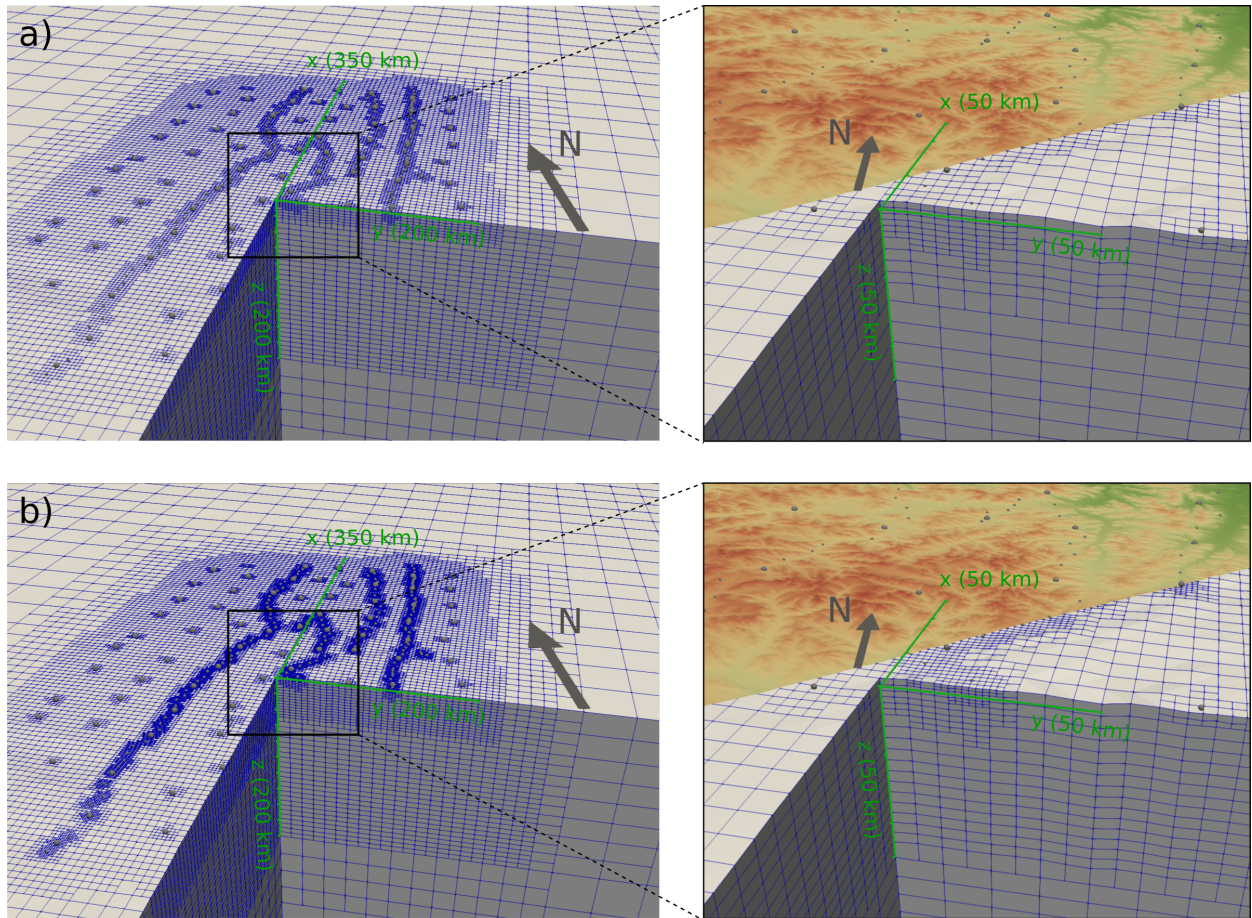
Figure 6. Cutaway view of the coarse (a) and fine (b) inversion meshes as well as a zoomed-in view of the central part. Local Cartesian axes (shown in green) are rotated by 15° clockwise from magnetic North.

3.4   Inversion methodology

We designed a multi-stage approach for inverting the data as shown by the flow-shart in Fig. 7. We start by inverting the regionally averaged 1-D impedance $\bar{Z}_{\text{1-D}}$, followed by the 3-D inversion with increasing number of sites and a wider period band. As illustrated in Fig. 7, the final result of each stage is used as the starting model for the subsequent stage, which is done with a finer mesh and more data.

The objective function (eq. 11) has multiple minima. To prevent the inversion from getting trapped in a local minimum that may not correspond to a geologically plausible model, the choice of the starting model is crucial. Rung-Arunwan et al. (2016) proposed to use a 1-D model derived from the regional 1-D impedance (eq. 7) as a starting model.
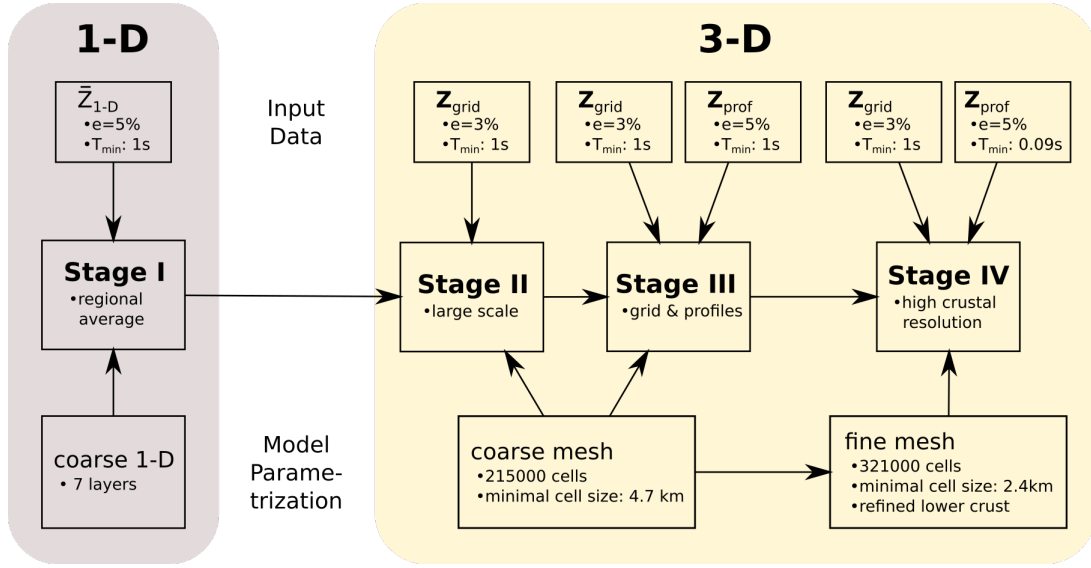
Figure 7. Flow chart of the inversion process, consisting of four stages with different model parametrizations and input data. $\bar{\bar{Z}}_{1\text{-}D}$ is the regionally averaged 1-D impedance (eq. 7), while $\mathbf{Z}_{grid}$ and $\mathbf{Z}_{prof}$ indicate the 2×2 impedance tensors from grid and profile sites (see Fig. 1). e corresponds to the assigned data error (eq. 13) and the shortest period is denoted by T_{min}.

To calculate the regional average, we used a stochastic inversion algorithm based on the Covariance Matrix Adaption Evolution Strategy (CMAES, see Grayver & Kuvshinov 2016), followed by a Markov chain Monte Carlo (MCMC) walk to evaluate its uncertainty. The obtained 1-D conductivity model is then used as an initial model for the 3-D inversion in Stage II.

For Stage II, only the 2×2 impedance tensors (with $T > 1$ s) from quasi uniformly spaced grid sites $\mathbf{Z}_{grid}$ (red sites in Fig. 1) are inverted. The resulting model is then passed on to Stage III, where 2×2 impedance data from the profile sites $\mathbf{Z}_{prof}$ (blue sites in Fig. 1) are added, most of which are telluric sites with inter-site impedance tensors estimated using the H-field from a nearby full MT station. Based on the result from this step, the final inversion step is performed with the finer mesh (further refinement in the lower crust) and impedances at shorter periods ($T > 0.09$ s). We found that this approach not only reduces computational costs compared to running the inversion on the fine mesh directly, but it also improves convergence significantly and enables the imaging of large and small scale structures within a single model.

4   RESULTS

4.1   Stage I: regional 1-D models

As outlined in Section 3.4, the regional 1-D impedances for sites north and south of the SHF (see Fig. 3) were inverted to obtain 1-D conductivity models (see Fig. 8). The model consists of seven homogeneous layers, consistent with the depth discretization of the 3-D mesh. The best fit models agree with the data well. As outlined in Section 2.3, $\bar{Z}_{\text{1-D}}$ derived from the southern sites is likely not representative of a regional conductivity structure. As a result, we used the 1-D model derived from the northern sites to be the starting model for the subsequent 3-D inversion of the whole region.
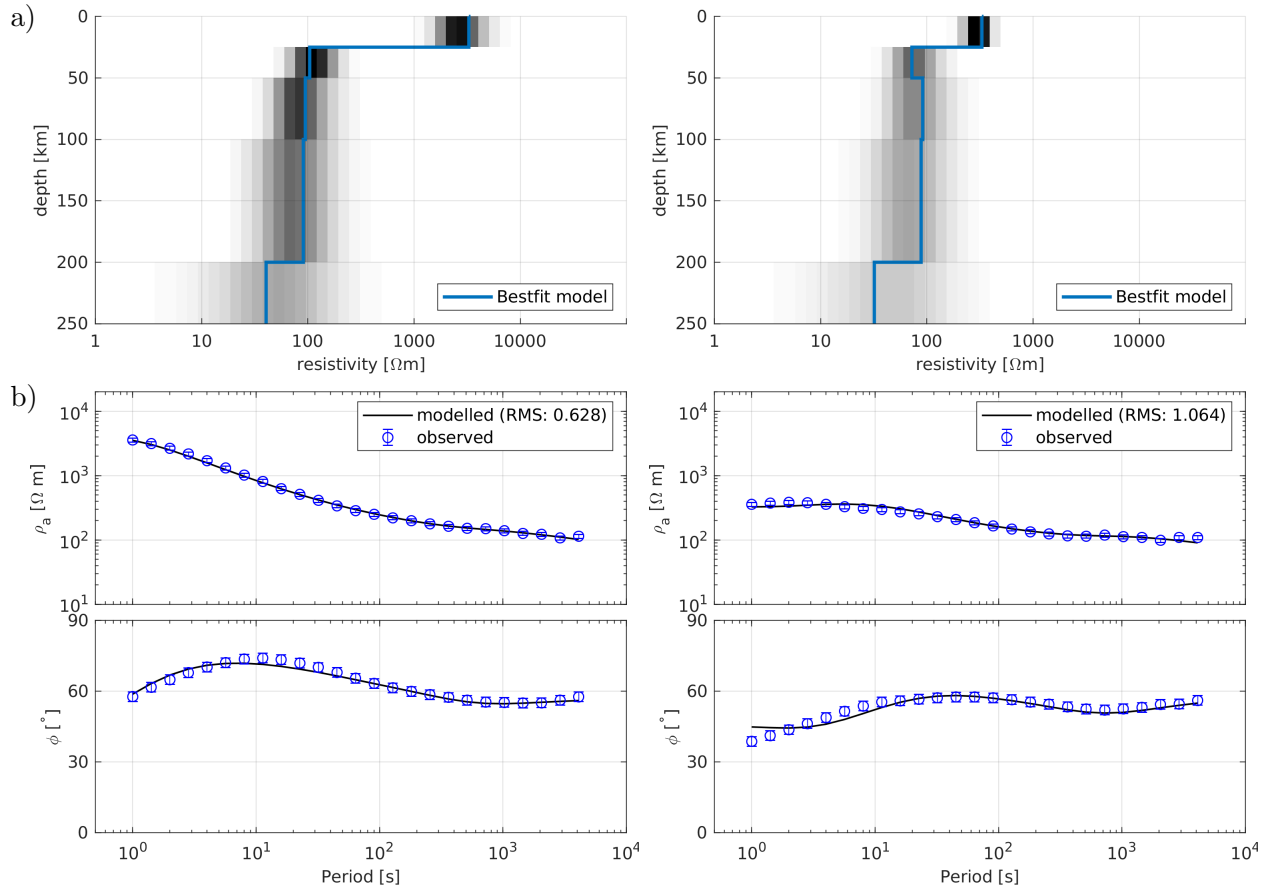

Figure 8. a) Regional 1-D conductivity models (blue), together with a distribution of equivalent models (grey shaded areas) for sites north (left panels) and south (right panels) of the SHF. b) Their data fit for sites north (left panels) and south (right panels) of the SHF.

4.2   Stage II: 3-D large-scale inversion

For this stage, only data from the grid sites (50 km nominal spacing) were inverted. Fig. 9 shows the progressive reduction of the data misfit (as defined by a root-mean squared misfit, RMS) and regularization parameter for each iteration step. As discussed in Section 3.2, the regularization parameter was decreased over the course of the inversion to permit more structure in the model. Starting from an RMS value of 43.1 using the initial 1-D model (see Section 4.1 and Fig. 8), the inversion achieved an RMS value of 2.65 after 19 iterations. Fig. 9a) shows an increase in the misfit for four out of the 19 iterations, indicating an escape from a local minimum or an overshoot, yet this did not prevent the inversion from converging. A continuation with even lower regularization resulted in negligible misfit reductions ($< 3\%$ per iteration) and therefore the inversion was terminated.

The best-fit model (model S2) is shown in Figs 10 and 11 (see Table 1 for abbreviations of geographic and model features). The upper crust is characterised by the resistive Hangai cratonic block (HB) north of the SHF and the very heterogeneous and generally conductive Valley of Lakes (VL) south of the SHF. The Bogd fault (BF) can be traced as a strong conductor. In contrast, the Bulnay and Gobi-Altai Faults (BUF and GAF respectively) are not clearly imaged. At depths of 30 to 35 km below the Hangai, there is an abrupt drop in resistivity of three to four orders of magnitude, most likely indicating a transition to the ductile lower crust. The lower part of the crust ($35 - 50$ km) is a heterogeneous conductor, labelled as North, East, South, and West Hangai Conductor (NHC, EHC, SHC, and WHC, respectively). The Valley of Lakes on the other hand is underlain by a resistor (VLR). In the upper mantle (below 50 km) and above the Asthenosphere (AS), resistivities are again higher, except for the SHC and EHC. They extend vertically from the lower crust to the AS.

The single RMS value of the best fitting model is not sufficient to judge its quality (Tietze & Ritter 2013; Miensopust 2017). Instead, the results were evaluated based on the convergence (see Fig. 9), data fit distribution over periods and site locations, as well as histograms of the residuals. Fig. 12 gives a detailed breakdown of the data fit. RMS values
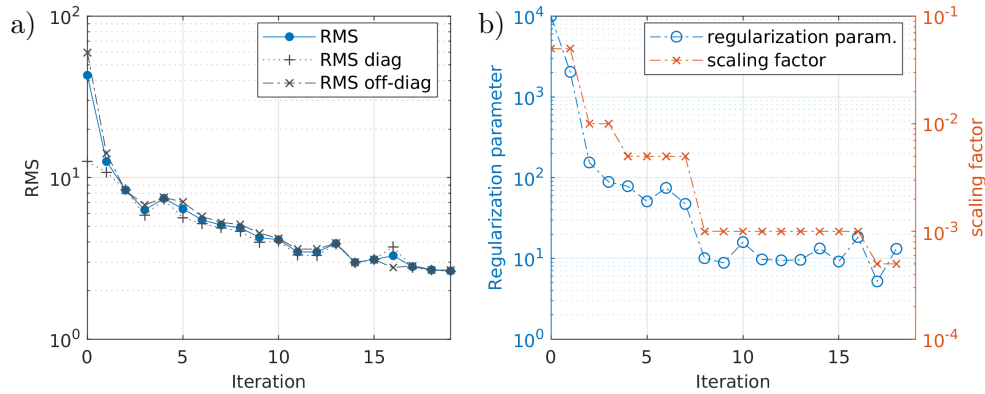
Figure 9. Progression of the RMS value (a) and regularization (see eq. 15) parameters (b) during Stage II of the inversion.

₃₈₉ are lowest over the period range from 10 s to 1000 s with slightly higher values for shorter and

₃₉₀ longer periods, likely because the coarse grid we use still does not allow the introduction of

₃₉₁ structures to fit the shortest periods, whereas long period data are typically more noisy (due

₃₉₂ to limited recording times) and difficult to fit. The misfit distribution over individual sites

₃₉₃ is relatively uniform in the central and northern parts but generally higher in the southern

₃₉₄ part. The southern part of the model is characterized by strong lateral resistivity variations

₃₉₅ in the VL and the conductive BF (see the surface panel in Fig. 10). Here, coarse model

₃₉₆ discretization and regularization prevented the introduction of stronger resistivity variations

₃₉₇ resulting in poorer fit, which we will improve at later stages. Static shift was largely corrected

₃₉₈ by the introduction of bow-tie shaped conductivity artefacts (see the surface panel in Fig.

₃₉₉ 10) close to the sites. Data residuals (see Fig. 12b) exhibit a symmetric and zero-centered

₄₀₀ distribution, indicating no data-fit pathologies at this stage. The relatively large variance of

₄₀₁ the distribution will be reduced at later stages.
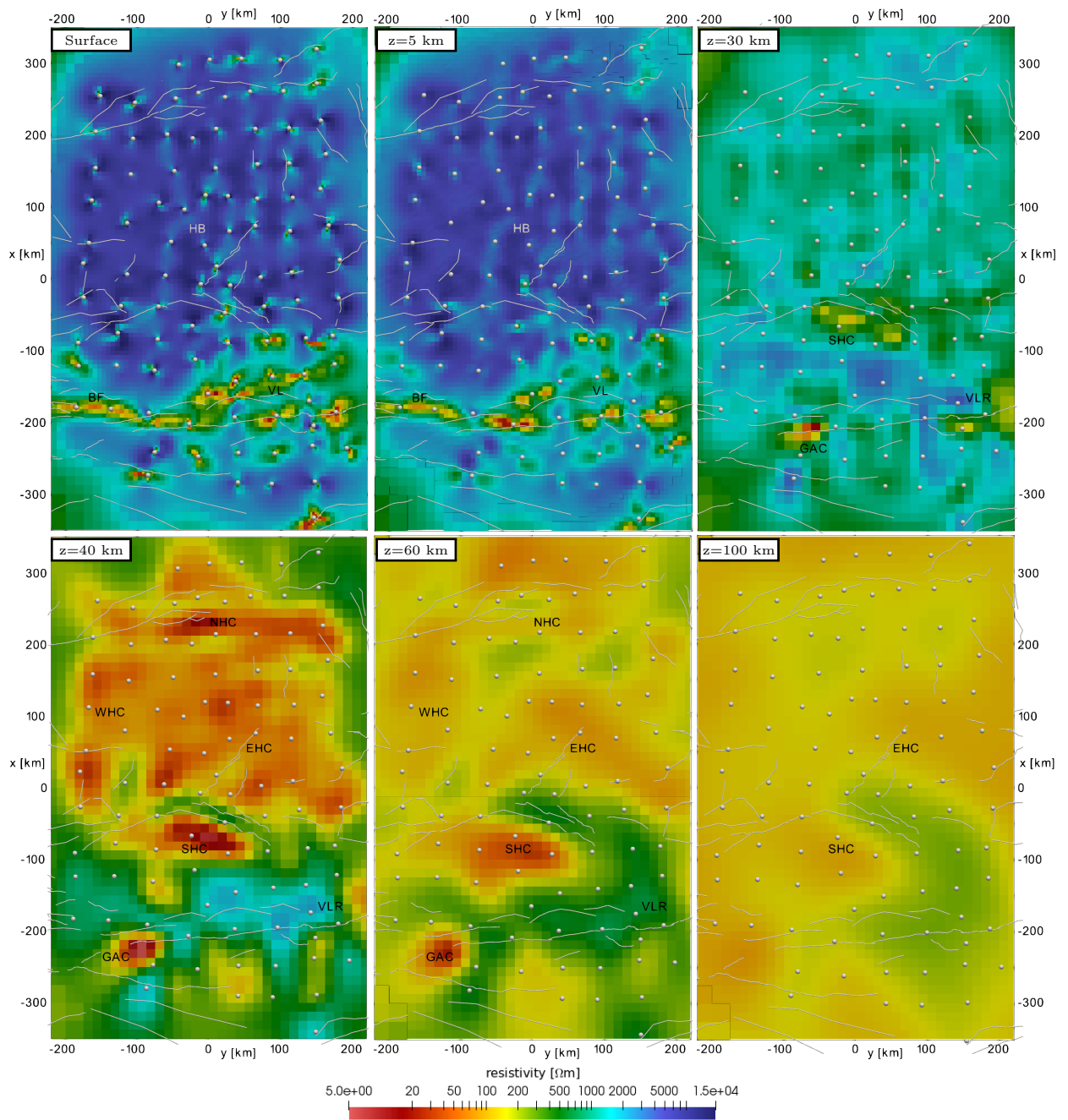
Figure 10. Horizontal slices through the best-fit model of inversion Stage II (model S2). Depth slices are shown at the surface and depths of $z = 5$ km, $z = 30$ km, $z = 40$ km, $z = 60$ km and $z = 100$ km (referred to sea level). Measurement sites are marked with grey spheres and major faults with grey lines. See Table 1 for abbreviations of model features, they include the resistive HB and the heterogeneously conductive VL with the BF in the upper crust. At a depth of 30 to 40 km the resistivity drops abruptly to form five distinct conductors in the lower crust and below, the SHC, NHC, WHC, EHC and GAC. Conversely, the VL is underlain by a resistor (VLR). With greater depths resistivity rises and at 100 km only the SHC and EHC remain discernible.
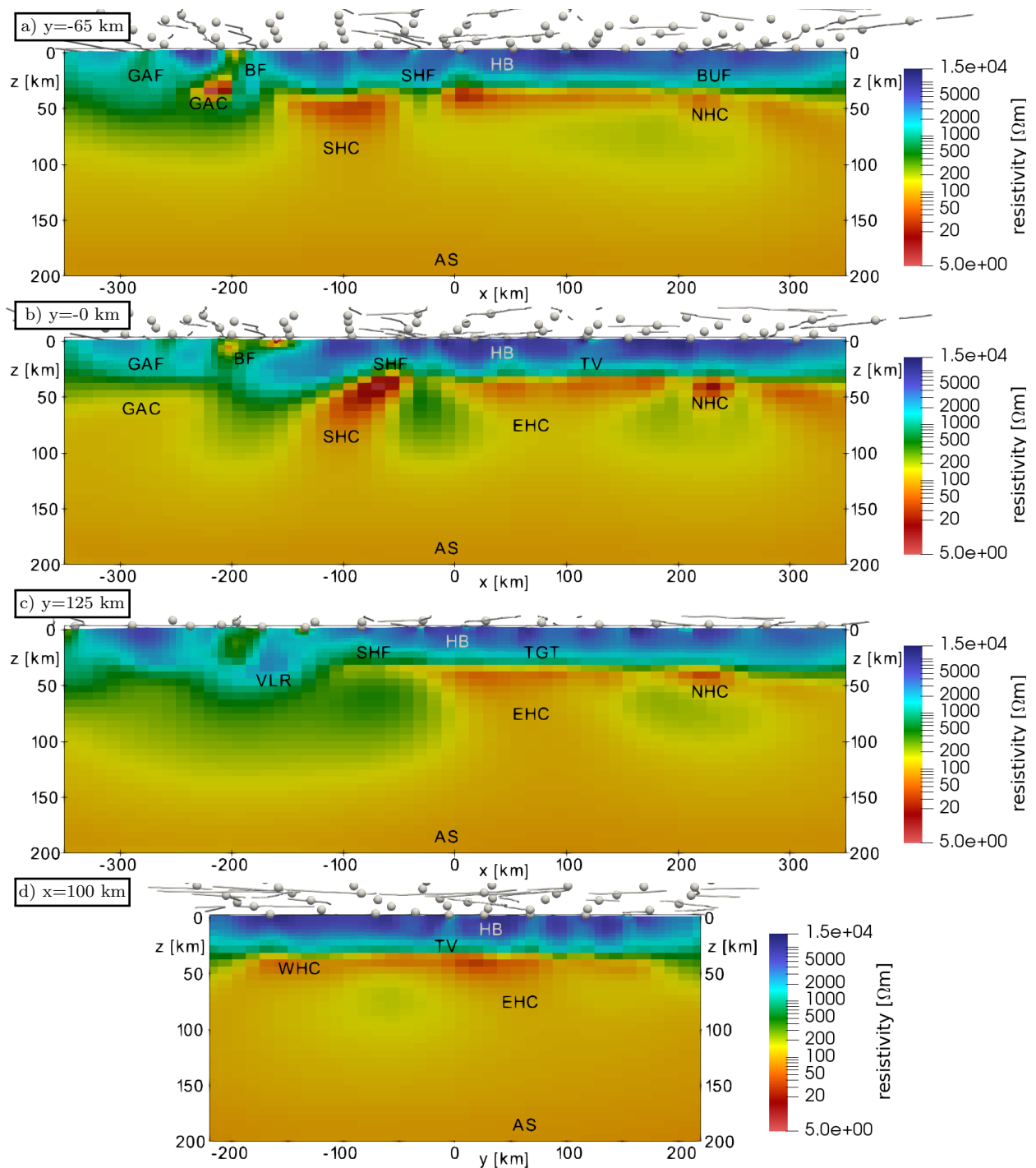
Figure 11. Vertical slices through the best-fit model of inversion Stage II (model S2). The slices are parallel to the x-axis at a) $y = -65$ km, b) $y = 0$ km, c) $y = 125$ km (approximately aligned with profiles 2, 4, and 6, see Fig. 1), and d) parallel to the y-axis at $x = 100$ km. Measurement sites are marked with grey spheres and major faults with grey lines. See Table 1 for abbreviations. The conductive BF can clearly be seen in the upper crust, whereas the GAF and SHF only show up as faint near-surface conductors. Additionally, it can be seen that the NHC is confined to a depth of 40 to 60 km (the lower-most crust), while the EHC and SHC extend downward to the AS. See also Fig. 10 for major model features.
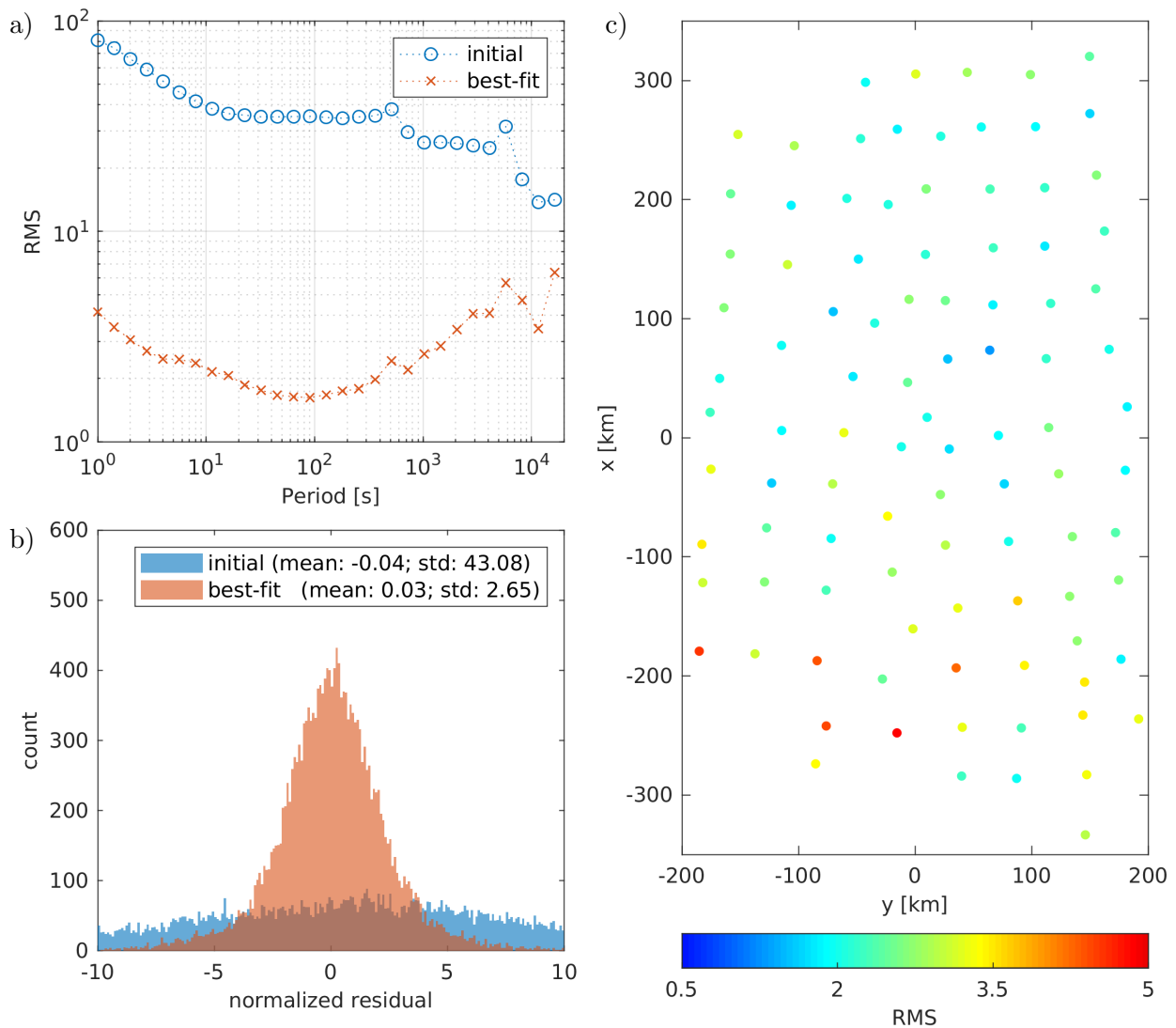
Figure 12. Data fit distribution of inversion Stage II. a) RMS value across periods for the initial and best-fit model; b) data residual histogram for the initial and best-fit model; c) RMS values at measurement sites for the best-fit model.

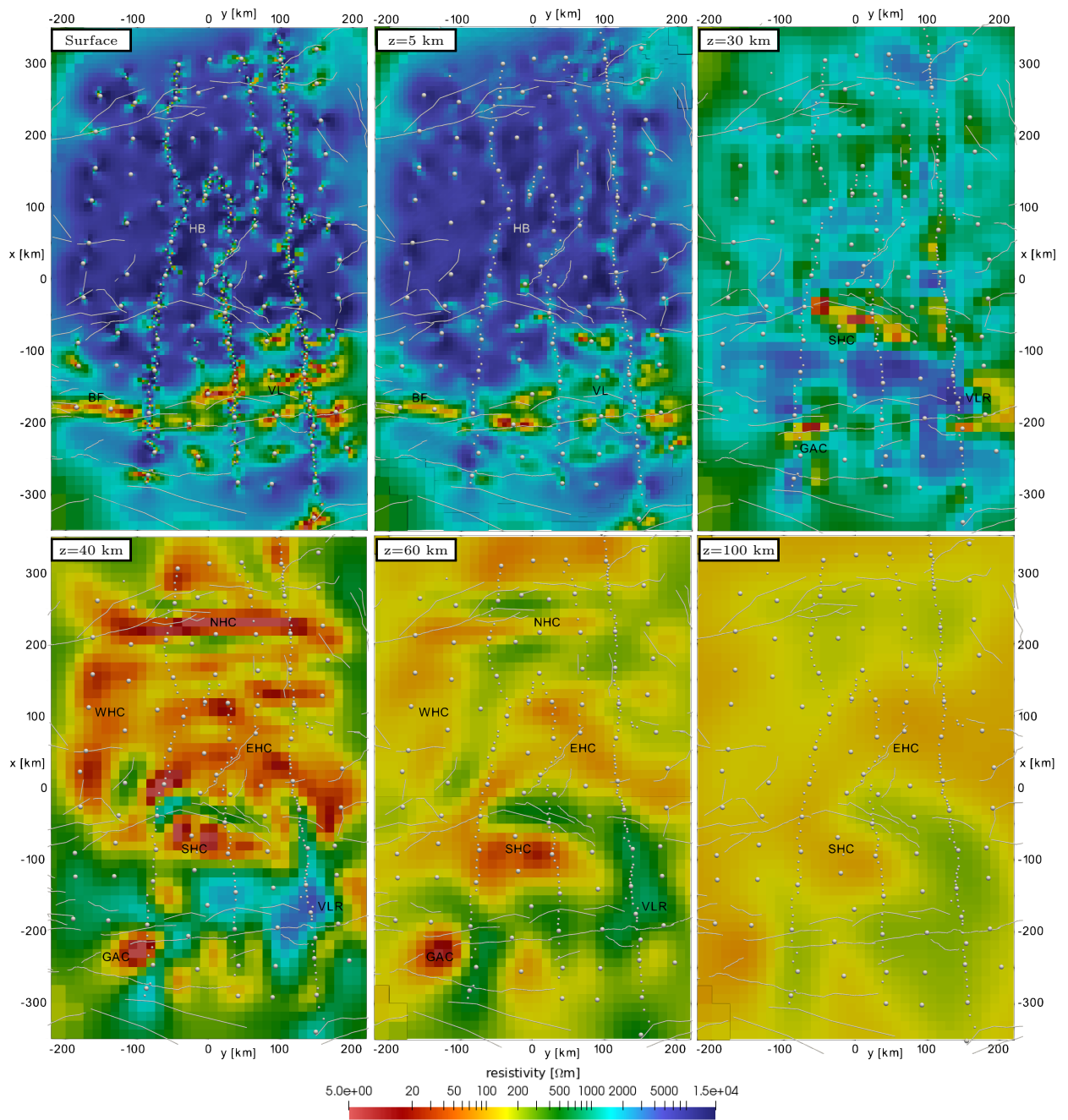## 4.3   Stage III: 3-D inversion of all measurement sites

For the third stage, all measurement sites along profiles and near the TV and TGT were included (mostly telluric-only data). Adding the new data to the previous best fit 3-D model increased the RMS value to 33. After 12 iterations the inversion converged to a model with a RMS value of 2.1. Fig. 13 shows that an RMS value of 3 was reached after only four iterations, owing mostly to the compensated static shift effect. The best fit model (model S3) is shown in Figs. 14 and 15. In comparison to the results from the previous stage (Figs 10
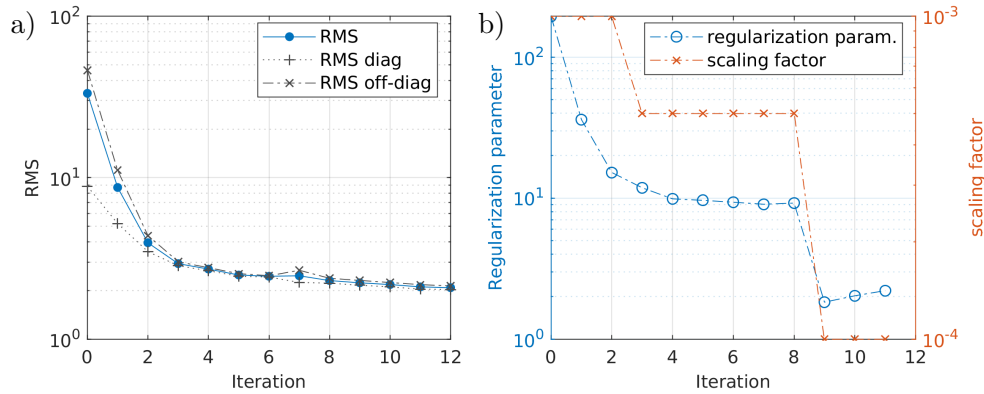
Figure 13. Progression of the RMS value (a) and regularization (see eq. 15) parameters (b) during Stage III of the inversion.

and 11), the large-scale structure remains the same, but resistivity contrasts became better resolved and some crustal structures appear more pronounced, such as the peculiar shape of the NHC. Additionally, the upper crustal resolution is improved (GAF, BF, and SHF) and new structures appear, for example the lowered resistivity in the upper crust below the TV and the TGT.

With a RMS value of 2.1, the data fit (Fig. 16) is overall better than in the previous stage, but with the same characteristics. Specifically, the misfit is slightly higher for short and long periods as well as for the southern sites. Additionally, there are three sites on profile P2 and two sites on profile P4 with a significantly higher misfit. These remaining problems are mainly due to the complex local 3-D structures and are resolved in the final stage of the inversion.

Figure 14. Horizontal slices through the best-fit model of inversion Stage III (model S3). Depth slices are shown at the surface and depths of $z = 5$ km, $z = 30$ km, $z = 40$ km, $z = 60$ km and $z = 100$ km (referred to sea level). Measurement sites are marked with grey spheres and major faults with grey lines. See Table 1 for abbreviations of model features. In comparison to the previous stage (see Fig. 10), model features are imaged more finely. The near surface along the profiles and the conductors in the lower crust ($z = 40$ km) especially benefit from the additional data included in this stage.
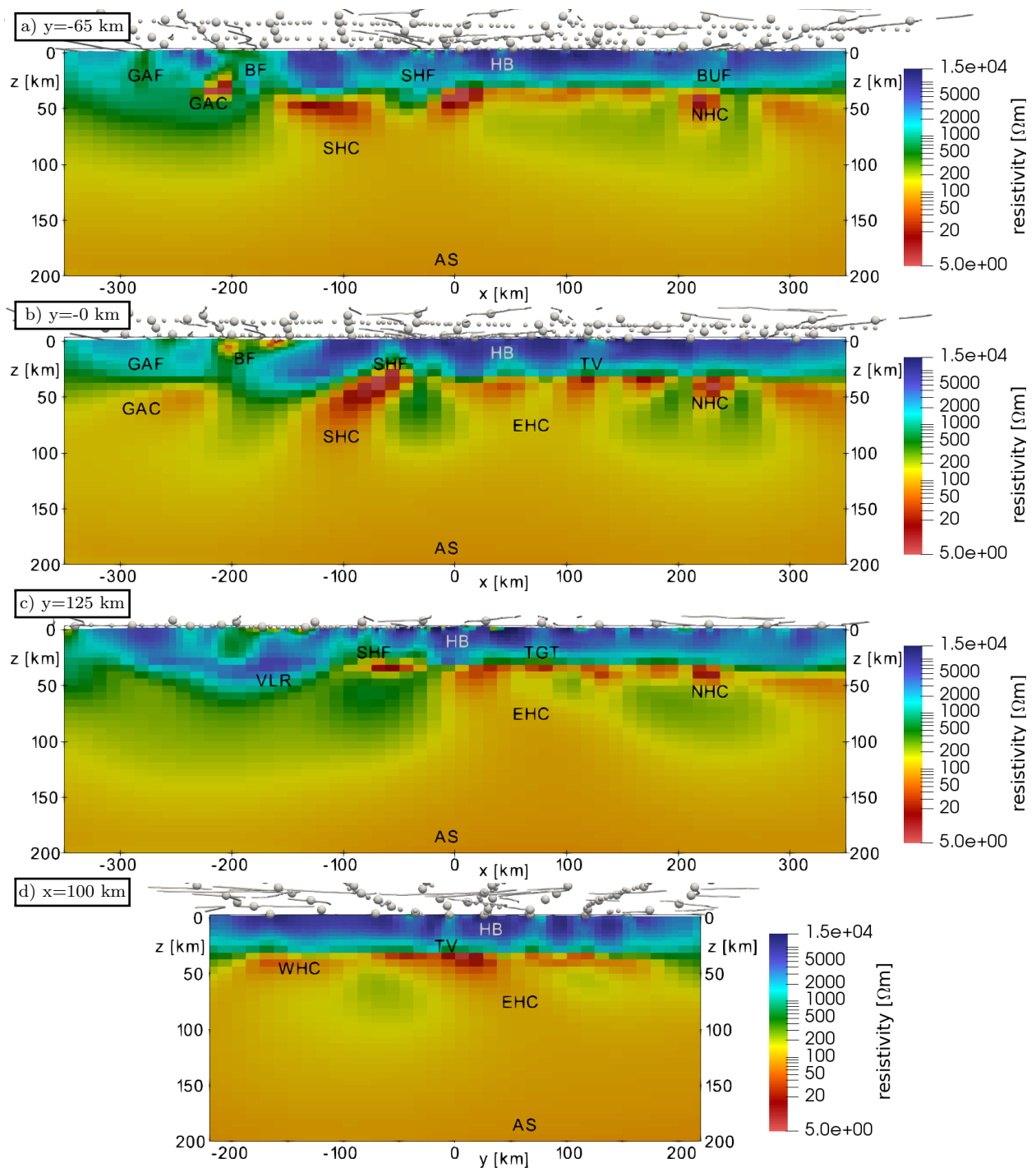
Figure 15. Vertical slices through the best-fit model of inversion Stage III (model S3). The slices are parallel to the x-axis at a) $y = -65$ km, b) $y = 0$ km, c) $y = 125$ km (approximately aligned with profiles 2, 4, and 6, see Fig. 1), and d) parallel to the y-axis at $x = 100$ km. Measurement sites are marked with grey spheres and major faults with grey lines. See Table 1 for abbreviations of model features. See Fig. 10 for major model features. In this model, conductive signatures can be seen in the upper crust below TV and TGT.
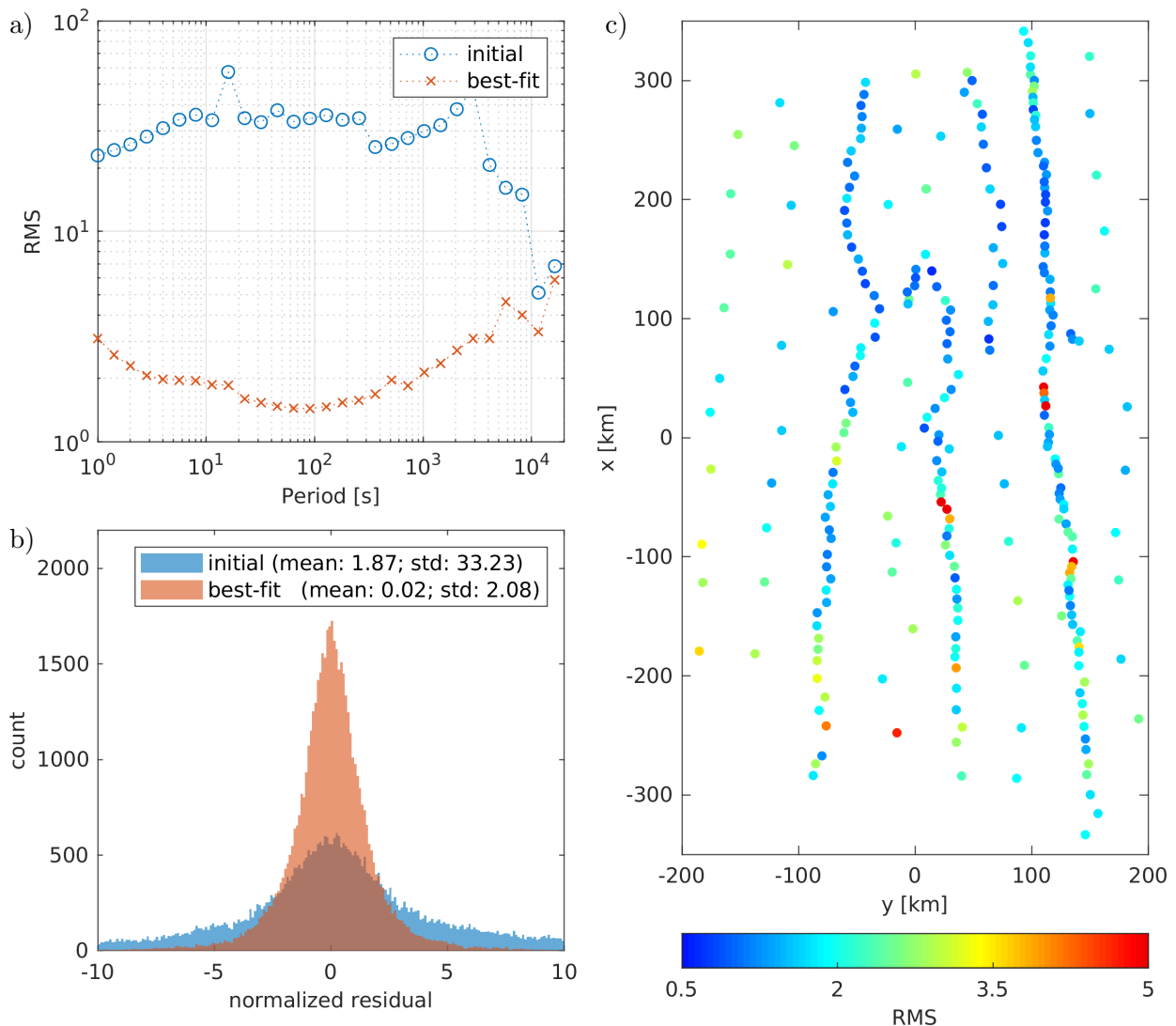
Figure 16. Data fit distribution of inversion Stage III. a) RMS value across periods for the initial and best-fit model; b) data residual histogram for the initial and best-fit model; c) RMS values at measurement sites for the best-fit model.

4.4   Stage IV: higher crustal resolution and short periods

For the last stage, short period data along the denser profiles were added and a finer mesh was used. As we will see, the mesh refinement around site locations and in the lower crust leads to a better fit for short period data.

Adding new data increases the RMS to a value of 8.9 when using the best fitting model from the previous stage. After 17 iterations a misfit of 1.86 was obtained (see Fig. 17). The resulting model (model S4) is shown in Figs 18 and 19. Compared to the previous stage,
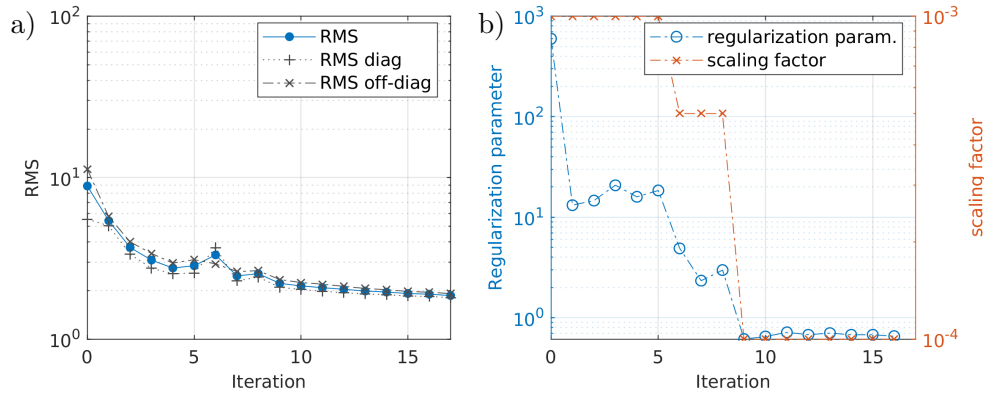
Figure 17. Progression of the RMS value (a) and regularization (see eq. 15) parameters (b) during Stage IV of the inversion.

the finer mesh leads to significantly improved resolution in the lower crust, which further enhanced the geometry and structure of the lower crustal conductors (NHC, EHC, SHC and WHC). By adding the short period data, the crust is imaged more finely and the resolution is close to that of the 2-D model by Comeau et al. (2018c).

The model fits the data well (Fig. 20). The overall higher misfit at longer periods ($>$ 1000 s, Fig. 20a) can be attributed to noisy long period data and the fact that the assigned error was likely too optimistic for these periods. Additionally, there are eight sites that have a RMS values > 3.5, either due to noisy data and poor fit of the diagonal impedance components or because of unresolved local structures.
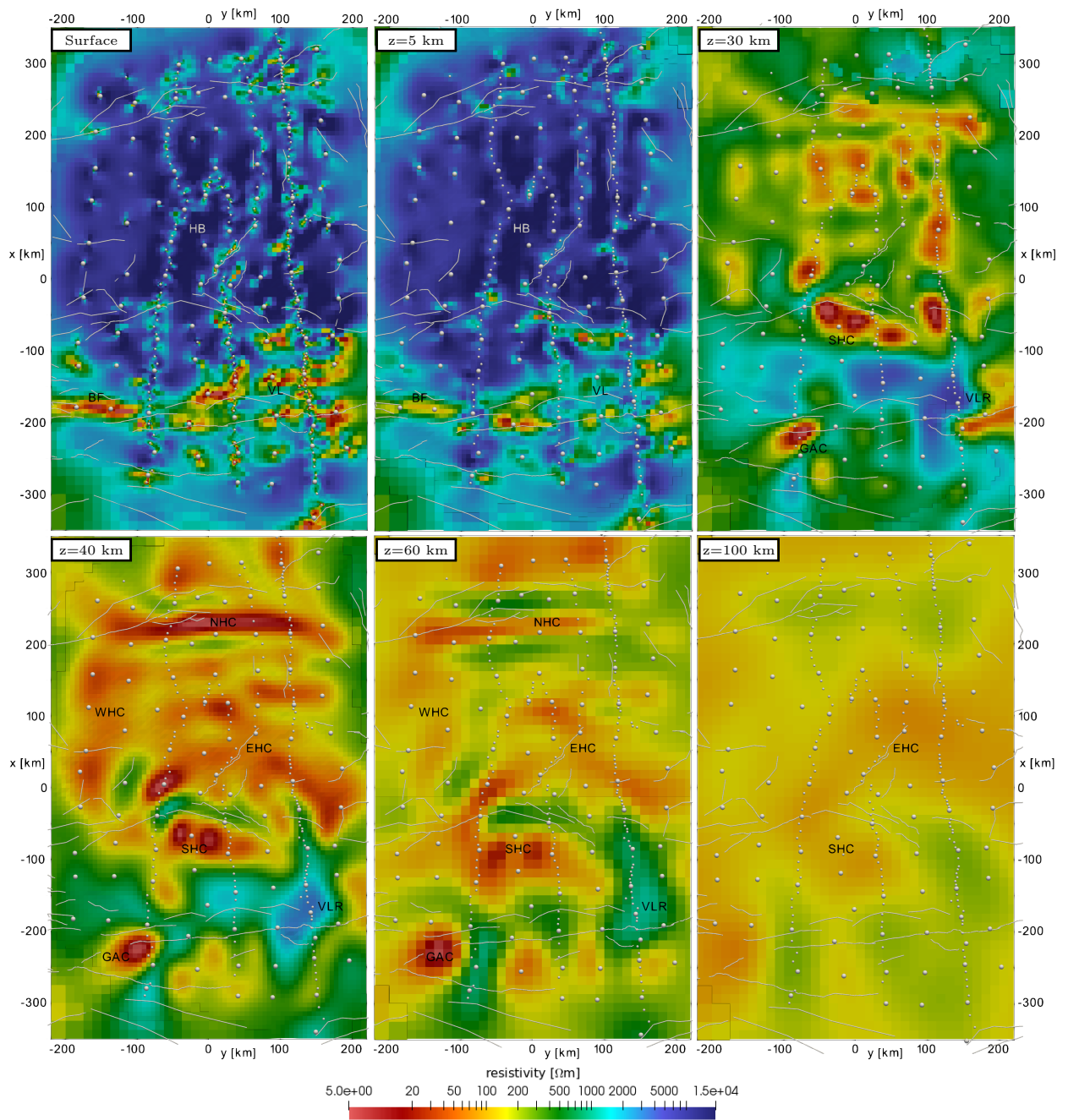
Figure 18. Horizontal slices through the final model of inversion Stage IV (model S4). Depth slices are shown at the surface and depths of $z = 5$ km, $z = 30$ km, $z = 40$ km, $z = 60$ km and $z = 100$ km (referred to sea level). Measurement sites are marked with grey spheres and major faults with grey lines. See Table 1 for abbreviations and Figs 10 and 14 for the model features.
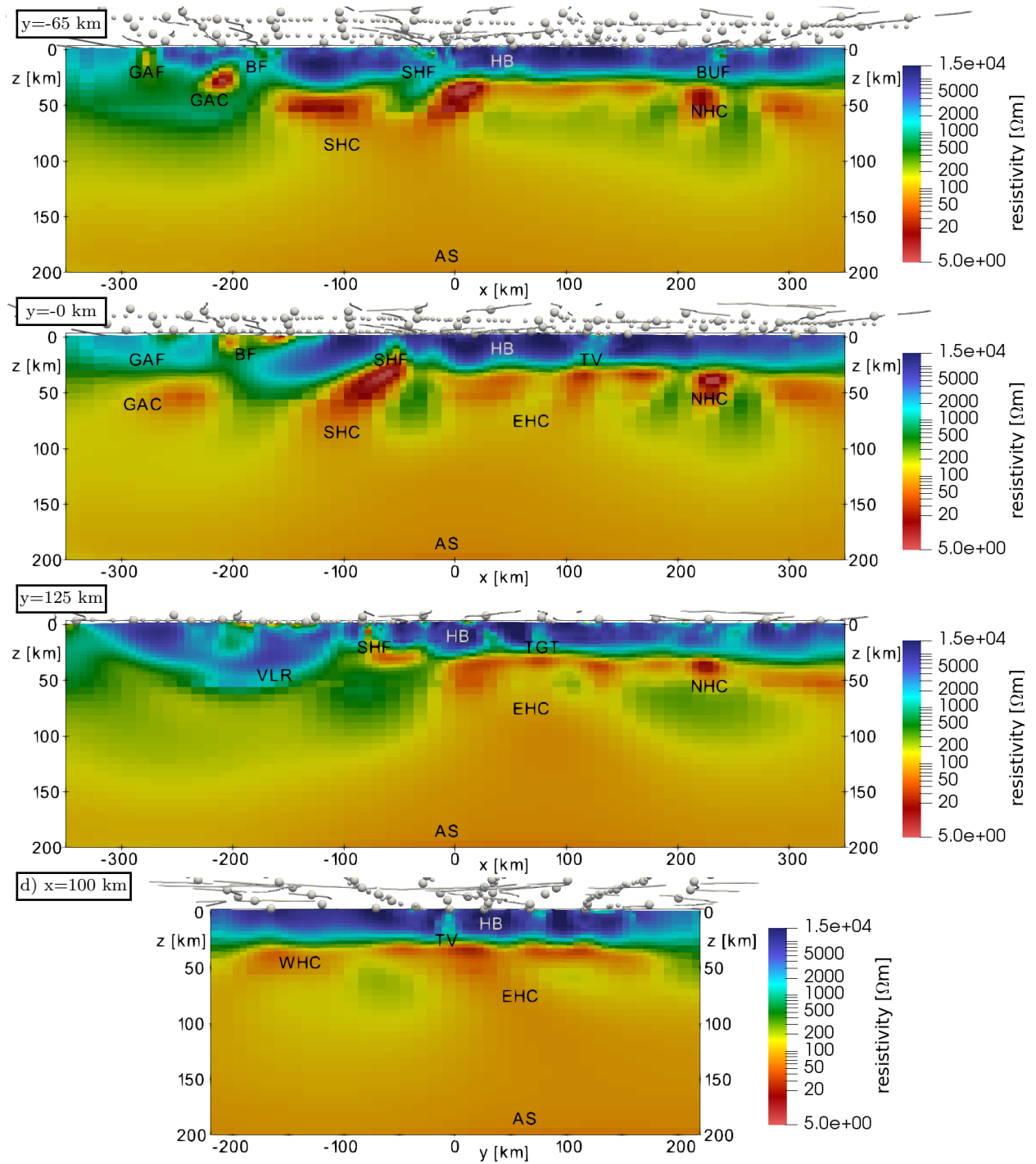
Figure 19. Vertical slices through the final model inversion Stage IV (model S4). The slices are parallel to the x-axis at a) $y = -65$ km, b) $y = 0$ km, c) $y = 125$ km (approximately aligned with profiles 2, 4, and 6, see Fig. 1), and d) parallel to the y-axis at $x = 100$ km. Measurement sites are marked with grey spheres and major faults with grey lines. See Table 1 for abbreviations and Figs 11 and 15 for model features. During this stage the BUF was resolved in some parts of the model.
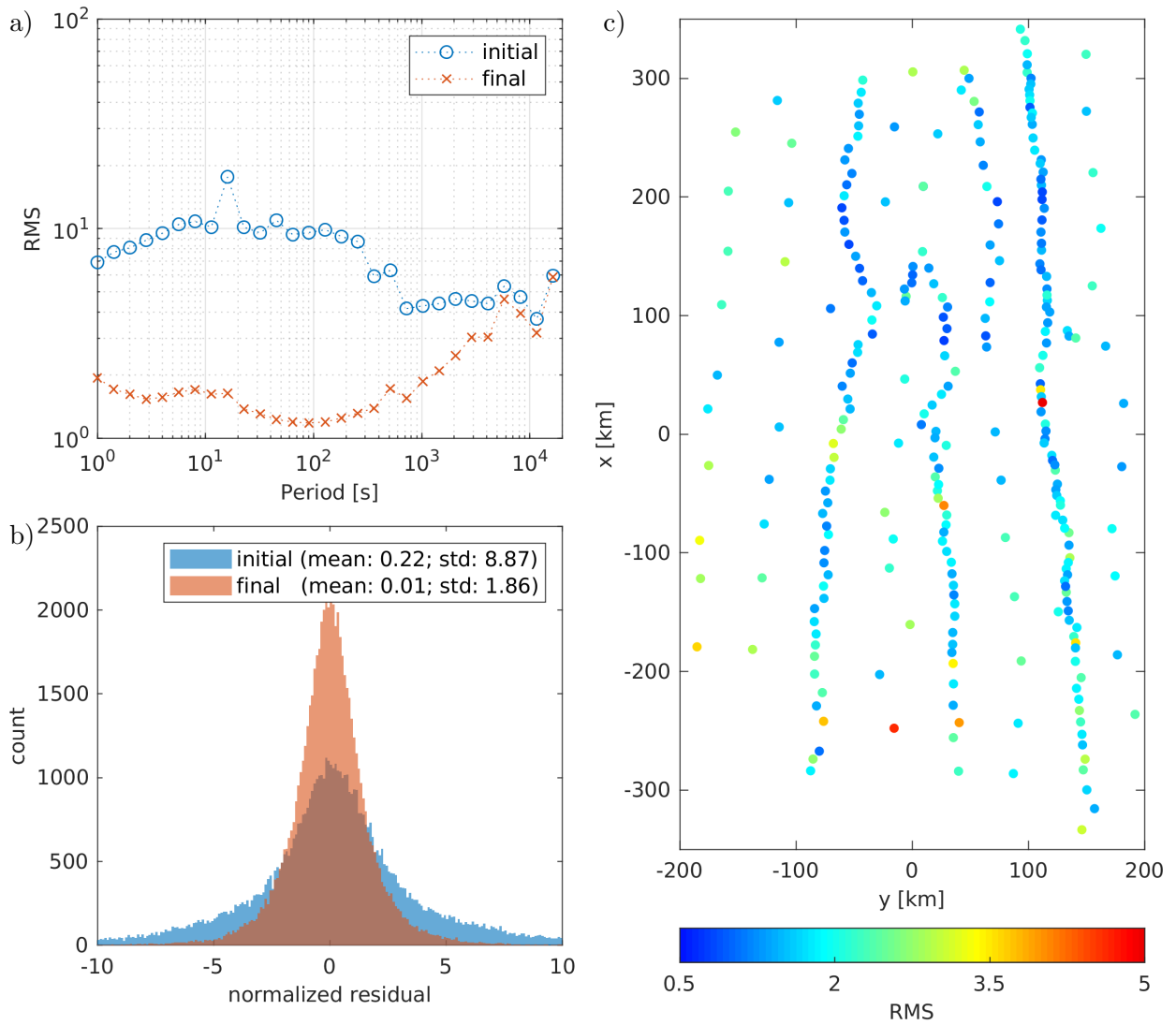
Figure 20. Data fit distribution of inversion Stage IV. a) RMS value across periods for the initial and final model; b) data residual histogram for the initial and final model; c) RMS values at measurement sites for the final model.

5   DISCUSSION

5.1   Inversion methodology

In the previous section, we explained the four stage inversion strategy used to obtain the final resistivity model. Fig. 21 shows a comparison of the models S2, S3, and S4 for an example area in the centre of the model. While larger features (HB, EHC, SHC, etc.) are already imaged in Stage II, the addition of profile sites during Stage III reveals smaller crustal features in more detail (SHF, TV, etc.) and gives a finer resolution for the structure of the EHC in model S3. Additional mesh refinement and the inclusion of short period data improves the results further, as is evident by the comparison of S3 and S4. The link between the SHC and SHF can be seen and TV becomes a prominent vertical conductor in the upper crust, located directly on top of a 40 Ωm conductor at a depth of 35 km. Similar improvements from stage to stage can be observed for other features throughout the model (e.g. TGT, GAF, BUF, BF, CV).

During the first stage, a regionally averaged 1-D model was derived to be used as an initial model for the 3-D inversion. It is well known that the initial model can significantly influence the result of a 3-D inversion. To assess the influence of the 1-D model, we performed two inversion runs with identical settings to Stage II except for initial half-space models of 500 Ωm (Model S2HS500) and 1000 Ωm (Model S2HS1000), see the supplementary material Sec. S3.1 and S3.2. After 18 iterations S2HS500 achieved a RMS value of 3.1 and S2HS1000 achieved a RMS value of 3.2 after 19 iterations. Both are significantly higher than the RMS value of 2.65 achieved after Stage II with a 1-D starting model (Sec. 4.2).

The recovered conductivity structure is similar to S2 only down to a depth of about 70 to 100 km. Below that depth no new features were introduced. Furthermore, it can be seen that the arbitrary choice of the initial half-space resistivity influences the overall resistivity of the final model, the average resistivity of S2HS500 is lower than that of S2HS1000. Although the initial 1-D model from Stage I has an influence on the results of Stage II, there is no arbitrary choice of resistivity values. Instead, the initial model is defined by the regionally averaged
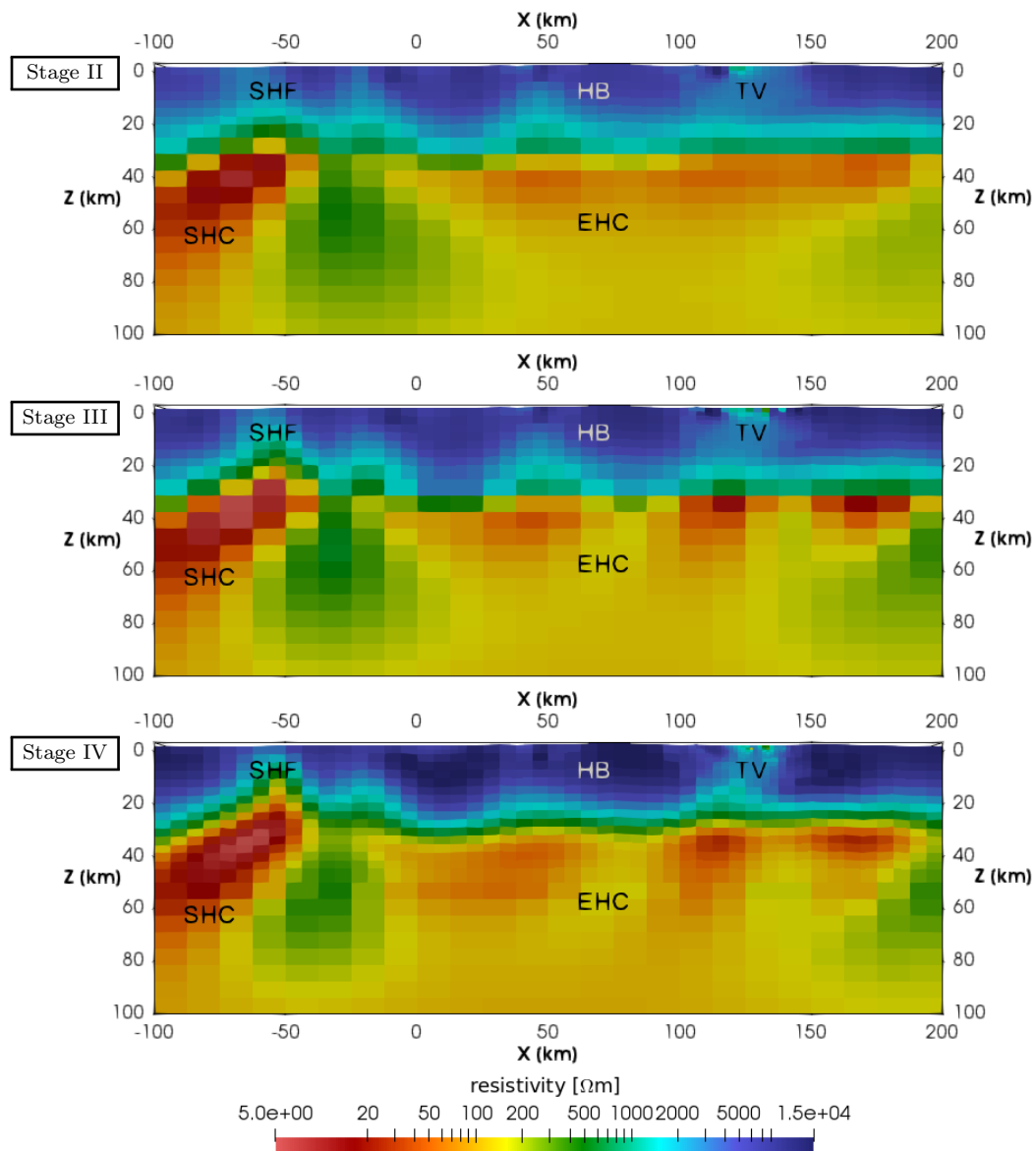
Figure 21. Comparison of the three stages of the 3-D inversion on a vertical slice in x-direction at $y = 0$. See Table 1 for abbreviations and Figs 11, 15, and 19 for major model features.

impedances and represents the best-fitting 1-D model, with the caveat that measurement sites south of the SHF were discarded (due to the lack of a consistent regional 1-D structure, as outlined in the Sections 4.1 and 2.3). The regional 1-D model north of the SHF is thereby imposed on the region in the south. However, this proves to be not a problem because the 1-D model enters Stage II only as an initial model, not as a reference for the regularization. The strong conductivity contrast at $z = 25$ km (see Fig. 8) is almost completely removed and a laterally more heterogeneous resistivity structure is introduced for the VL and the region south of the SHF to fit the data there.

471 Seperate inversion Stages II and III were necessary to ensure that the regional resistivity

472 structure was recovered first, before smaller and shallow structures were fitted. If the Stages

473 II and III are combined (see Model S2+3 in the supplementary material S3.3) the inversion

474 is strongly biased to the eastern part of the grid (between P2 and P6, see Fig. 1) due to the

475 higher number of stations there. This leads to the western part of S2+3 (west of P6) being

476 fitted only in the end of the inversion process (starting at iteration 15 of 23), resulting in

477 a significantly higher RMS value for sites along line 8, in comparison with the entire grid.

478 The recovered model happens to be virtually identical to model S3. However, because of the

479 bias to the eastern sites for most of the iteration steps, a separated approach is preferred,

480 whereby the regional 3-D structure is recovered from the grid stations first, and afterwards

481 smaller structures are revealed due to the additional data from the profiles introduced during

482 Stage III.

483 For the same reason, short period data (0.09 s to 1 s) with penetration depths as small

484 as 2 km were added in Stage IV, the final stage of the inversion process. The short period

485 data were accompanied by a mesh refinement, which increased the computational cost of

486 a single iteration by a factor of 2.4. By fitting the regional structure on the coarser mesh

487 first and using the fine mesh only in the end, the computational cost for the entire inversion

488 process was significantly reduced.

5.2 Description of observed features

5.2.1 Upper mantle features

491 The final 3-D resistivity model images a pervasive low-resistivity feature (30–100 Ωm) at

492 depths greater than 150 km (AS; see Figs 19 and 22). To the south, below the South Gobi

493 region, this feature appears at depths of approximately 130 km. Whereas below the Hangai

494 Dome, this feature appears to shallow to depths of approximately 70 km (SHC and EHC;

495 see Figs 19 and 22). This is consistent with previous 2-D models (Comeau et al., 2018c;

496 Comeau et al., 2019b). However, what is unique in the 3-D model presented here is that the

497 non-uniformness and lateral complexity of the feature is imaged. This low-resistivity feature

has two regions that shallow and bulge upwards: one region below the eastern Hangai Dome (EHC; see Fig. 22) that dips eastward, and a smaller region located slightly south of the Hangai Dome (SHC; see Fig. 23).

Previous seismic profile measurements indicated an irregular, dome-shaped lithosphere-asthenosphere boundary (LAB) below central Mongolia that varies from 70–130 km depth (Petit et al. 2008), and a deep ($<$ 150 km) low-velocity zone below the eastern Hangai (Chen et al. 2015; Zhang et al. 2017). Bouguer gravity models revealed a localized low-density structure at a depth of 80–125 km below the central Hangai (Tiberi et al. 2008, see Fig. 1). Furthermore, analysis of erupted xenoliths from intraplate volcanism in central Mongolia suggests long-lived ($<$ 30 Ma) and shallow ($<$ 70 km) melting of an asthenospheric source (Ionov 2002; Barry et al. 2003; Hunt et al. 2012).

Broad array coverage and the inclusion of long-period data in the resistivity model yield sensitivity to the asthenosphere (confer Fig. 3). Based on the available evidence, the deep, low-resistivity feature may be explained by a non-uniform LAB with small, localized up-wellings. The moderate resistivity values observed in the final model can be explained by low-percent partial melts (Comeau et al. 2018c), possibly generated by decompression melt-ing from a small-scale asthenospheric upwelling. Comeau et al. (2018c) calculated more than 3% melt was required to explain the resistivity values observed in the mantle, consistent with geochemical estimates of 2–7% from lava samples (Hunt et al. 2012; Ancuta et al. 2018).

The EHC lies below the eastern Hangai Dome, a region of elevated topography and the location of many Cenozoic volcanic provinces (Ancuta et al. 2018, see Fig. 1), elevated heat-flow measurements (Ionov 2002, and references therein, see Fig. 1), and a high concentration of present-day hydrothermal activity in the form of meteoric hot springs (Ganbat & Demberel 2010; Oyuntsetseg et al. 2015, see Fig. 1). In contrast, in the western part of the Hangai Dome, despite its topographic similarity to the eastern part, there are few signs of volcanism and hydrothermal activity. The SHC lies below a topographic high slightly south of the Hangai Dome. Both the EHC and SHC are connected with a continuous low-resistivity region below 150 km. It is not known whether there exists similar regions, for example

below the Hovsgol rift and volcanic region in northern Mongolia, and if so, how they are connected at depth.

The origin of a small-scale asthenospheric upwelling remains purely speculative at this time. Historically, explanations for intra-continental uplift have been dominated by arguments for hot, mantle-rooted plumes (e.g. Windley & Allen 1993). However, modern geophysical and petrological evidence in central Mongolia is not consistent with this explanation (e.g. Barry et al. 2003). Alternative explanations include edge-driven convection resulting from a lithospheric step near the Siberian Craton that could cause thermal erosion of the lithosphere (as in Bao et al. 2014), or thinning of the lithosphere by a delamination process, whereby dense sub-crustal lithosphere decouples and peels away from the crust (Bird 1979; Kay & Kay 1993; Meissner & Mooney 1998). The latter explanation may account for other observational constraints in central Mongolia, such as the intracontinental uplift of the Hangai Dome and the long-lived mantle melting responsible for intraplate volcanism. Furthermore, numerical modelling studies indicate that a weak lower-most crust is required to trigger a delamination event (Krystopowicz & Currie 2013), consistent with observations in central Mongolia (see below; Vergnolle et al. 2003).

5.2.2 Lower crustal structure

The final 3-D resistivity model images a prominent, heterogeneous low-resistivity zone (5–50 Ωm) in the lower crust (30–50 km; NHC, WHC, EHC, and SHC in Figs 18 and 19). It is well-resolved because it is overlain by a highly-resistive feature (> 2000 Ωm; HB) and is a robust modelling result at all inversion stages (see Fig. 21). This feature is pervasive throughout the central Hangai but ends abruptly at the South Hangai fault zone (SHF; see Fig. 19). In the northern Hangai region this heterogeneous low-resistivity zone is roughly organized into several east-west trending tubes (e.g., NHC; see Fig. 18), roughly parallel to the Bolnay fault zone. The tube-like conductors (< 50 Ωm) have a nearly equal width and separation of approximately 25 km.

Crustal low-resistivity zones can be explained by local accumulations of conductive fluids
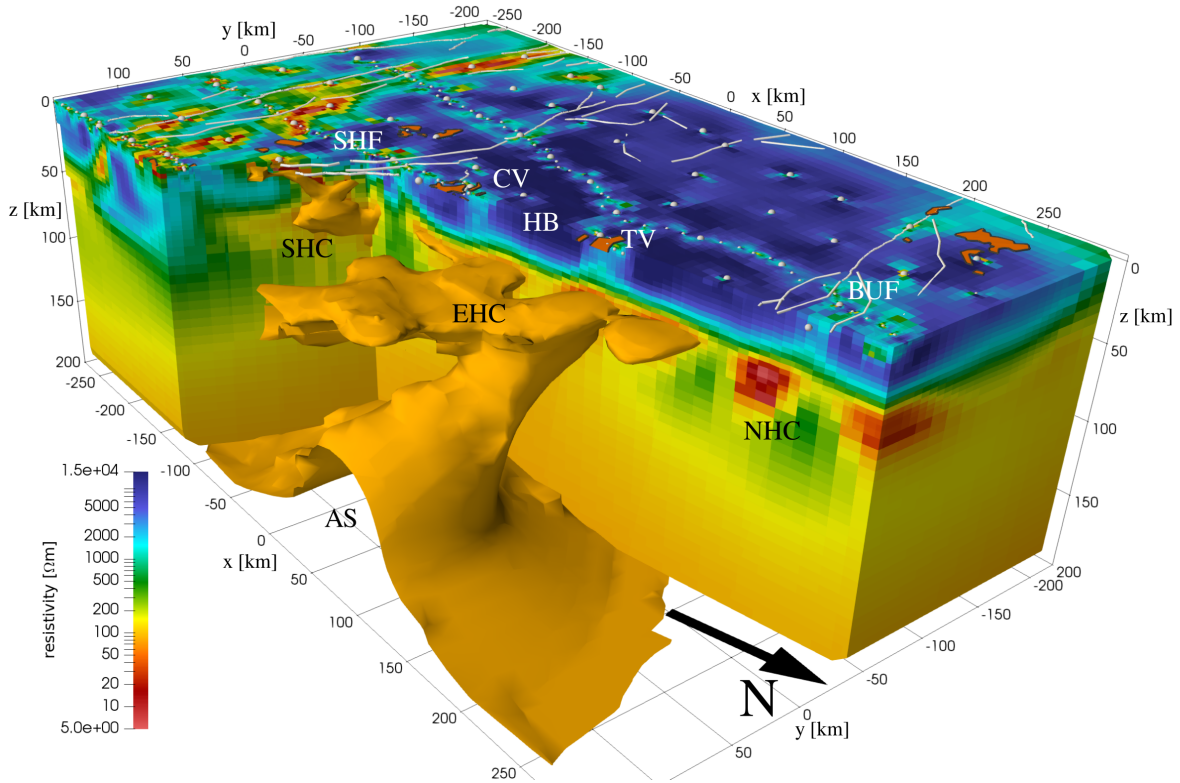
Figure 22. 3-D cutaway view of the model S4. The EHC and the eastern arm of the asthenospheric upwelling are shown with a 85 Ωm isosurface. White spheres indicate measurement sites, white lines are faults, and volcanic provinces are orange.

(e.g. Unsworth & Rondenay 2013). Geochemical evidence indicates that lithospheric metasomatism occurred in Mongolia due to the closure of the Mongol-Okhotsk ocean (Sheldrick et al. 2019) and highly saline fluids can be exsolved by metasomatism in dehydration and devolatilisation reactions (Manning 2018). Fluid content substantially changes the rheology and significantly reduces crustal strength and viscosity (e.g. Liu & Hasterok 2016). This is consistent with evidence from post-seismic slip measurements that indicate a significantly reduced viscosity in the lower crust of Mongolia, of several orders of magnitude, as compared to the upper crust (Vergnolle et al. 2003).

The location of these low-resistivity zones can be explained by a conceptual model that predicts that in compressive tectonic settings (as in central Mongolia) an inverted stress gradient beneath the brittle-ductile transition causes fluids to become trapped in the lower crust (Connolly & Podladchikov 2004). Furthermore, numerical hydromechanical models can
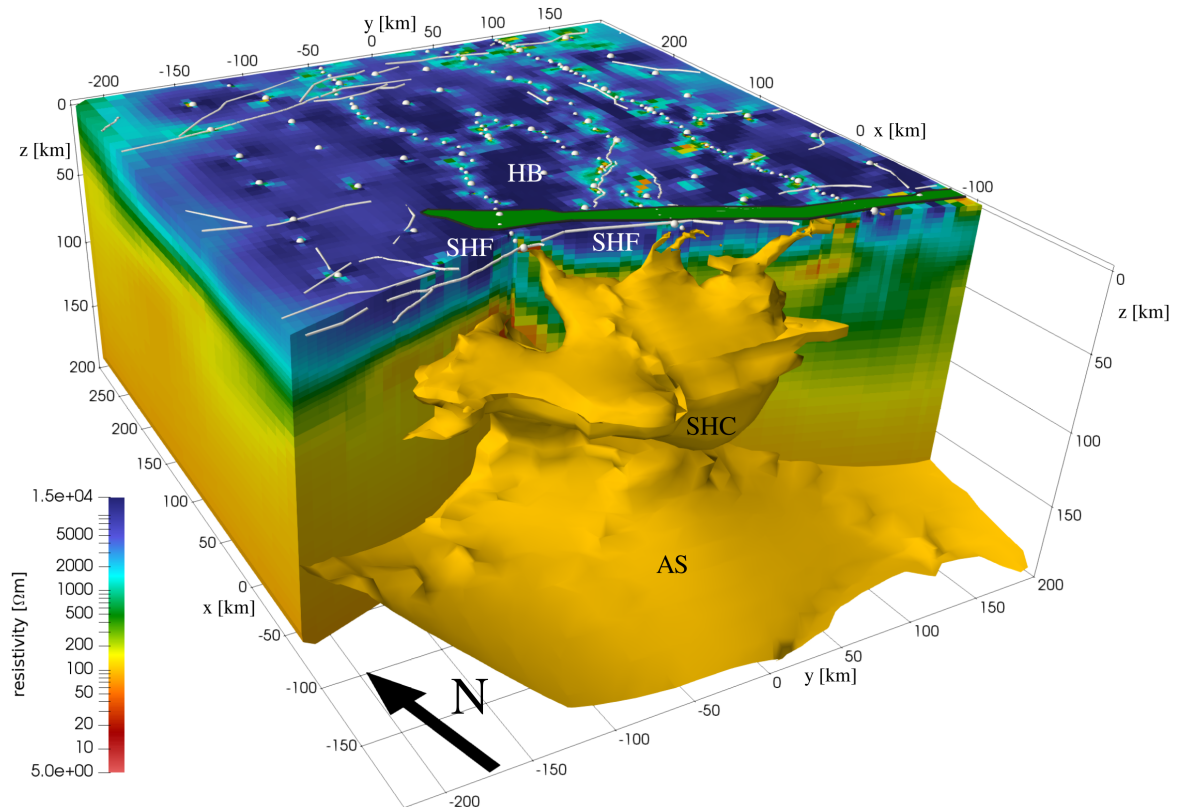
Figure 23. 3-D cutaway view of the model S4. The SHC and the southern arm of the asthenospheric upwelling are shown with a 100 Ωm isosurface. White spheres indicate measurement sites, white lines are faults, and the green area is the Bayankhongor Ophiolite Belt (Buchan et al. 2001).

explain how spatial focusing of the fluid source flux can create hydraulically connected, fluid-rich domains within the ductile crust (Connolly & Podladchikov 2013; Comeau et al. 2019a). In addition, the pattern of fluid focusing is expected to be superimposed on large-scale tectonic deformation patterns. Therefore, in central Mongolia such fluid-domains should form extended tubes aligned with tectonic block motion, compatible with what is observed (e.g. Calais et al. 2003). It is currently unknown how these low-resistivity tube-like features change northwards across the Bolnay fault zone and eastwards outside the Hangai block.

5.2.3   *Upper crustal structure*

5.2.3.1   Fault zones and terrane sutures   In general, the upper crust below the Hangai Dome is highly resistive ($2000 - 20000$ Ωm, HB in Figs 18 and 19). This can be explained by a pre-Cambrian, cratonic basement (Cunningham 2001). To the south in the VL, the near-

576 surface layer (< 1 km) has a highly variable resistivity (10 − 2000 Ωm) This is consistent

577 with porous sediments in an internal drainage basin between the Hangai and Altai mountains

578 (Cunningham 2001; Ganbat & Demberel 2010).

579 In the resistivity model, several anomalous low-resistivity upper crustal features are

580 imaged. To the south of the edge of the Hangai Dome a strong crustal conductor (20–

581 100 Ωm; SHF in Fig. 23) is imaged in several disconnected fragments trending roughly

582 east-west. This conductive feature was previously identified by Comeau et al. (2018c). It

583 extends towards the mid-crust and appears to connect with the SHC at depth.

584 Segments of the SHF system (Cunningham 2001; Walker et al. 2007), which marks a

585 terrane boundary (Badarch et al. 2002) and may be an ancient suture zone created during

586 the closure of the Mongol-Okhotsk ocean (Van der Voo et al. 2015), are congruent with many

587 of these anomalies. Fault zones are often regions of fractured, weakened crust that may have

588 circulating fluids, which increase their conductivity (Unsworth & Bedrosian 2004). Thus,

589 this could offer a potential explanation for these conductive anomalies. What is more, the

590 lower crustal conductive zone (discussed above in Sec. 5.2.2) terminates abruptly at this

591 zone, indicating the importance of this location as a major crustal boundary.

592 To the north, the resistivity model shows low resistive anomalies (50–100 Ωm; BUF in

593 Figs 19 and 22) at shallow depths (< 1 km) that become moderately resistive (200–1000 Ωm)

594 to depths of approximately 10 km and do not connect to lower crustal low-resistivity zones.

595 They are long, semi-continuous features that trend roughly east-west.

596 They appear to be coincident with the surface traces of the eastern segments of the

597 Bulnay fault zone (Calais et al. 2003; Rizza et al. 2015, see Fig. 22). As above, conductive

598 anomalies such as these can often be explained by fault zones. However, at mid-crustal

599 depths a strong conductive feature is not imaged. One explanation for why an electrical

600 signature could be absent from the lower reaches of a fault zone is that the fault is dry

601 and locked, often the case for fault zones with large and infrequent ruptures (Unsworth &

602 Bedrosian 2004), as is the case for the Bulnay fault zone (Rizza et al. 2015).

603 To the south, the model images a set of east-west trending anomalies (BF and GAF in

604 Figs 18 and 19). They have a low-resistivity (20–100 Ωm) to depths of approximately 20 km,

605 and are surrounded by otherwise highly resistive crust (> 1000 Ωm). In the southwest of

606 the model there is an isolated low-resistivity anomaly (5–50 Ωm; GAC in Figs 18 and 19)

607 at a depth of 10–25 km.

608   At the northern edge of the Gobi-Altai mountains runs a large fault zone known as the

609 Bogd fault that has been responsible for several large rupture events, including a moment

610 magnitude of 8.1 in 1957 (Walker et al. 2007; Rizza et al. 2015). Furthermore, this fault

611 zone represents a significant terrane boundary (Badarch et al. 2002). The Gobi-Altai fault

612 zone runs along the south of the Gobi-Altai mountain plateau (Calais et al. 2003; Walker

613 et al. 2007). The contrasting properties observed across this zone may reflect the rheological

614 differences between accreted terranes of different origins (see Guy et al., 2015 and refer-

615 ences therein; Comeau et al., 2019b). Again, the location of the low-resistivity anomalies is

616 coincident with these fault zones, and they offer a potential explanation for these features.

617 **5.2.3.2   South Hangai mineral zones**   Anomalous, strongly conductive features (10–

618 40 Ωm) stretch from the surface to the mid-crust near the South Hangai Fault zone (SHF;

619 see Fig. 23). They are subvertical, dipping slightly southwards.

620   Near the SHF is the Bayankhongor Ophiolite Belt (green area in Fig. 23) and the

621 Bayankhongor Metallogenic Belt, which is an economically significant ore zone that includes

622 important sources of gold and copper (e.g. Buchan et al. 2001). Many of the conductive

623 anomalies are coincident with known mineral deposits (Comeau et al. 2018b). Furthermore,

624 mineralization zones commonly have conductive signatures from associated sulfide mineral-

625 ogy and related metamorphic processes (e.g. Unsworth & Bedrosian 2004). Therefore, the

626 anomalous conductors may be explained by zones of mineralization.

627 **5.2.3.3   Tariat and Chuluut volcanic zones**   Anomalous moderately resistive features

628 (300–1,300 Ωm) are imaged within the homogeneous and highly resistive upper crust (>

629 2000 Ωm; HB) below the Tariat and Chuluut regions (TV and CV, along P4; see Figs 19

630 and 22). These anomalous features are vertically extended through the crust and sit above

a deeper (>70 km) bulging conductor, described above in section 5.2.1. Similar features are seen in the eastern Hangai below Tsenkher geothermal area (TGT in Fig. 19).

These regions are well-known volcanic zones. In fact, central Mongolia contains many volcanic provinces related to intraplate, alkaline basaltic volcanism (Barry et al. 2003; Hunt et al. 2012; Ancuta et al. 2018, see Fig. 1 for locations). The Tariat region is the youngest volcanic zone in central Mongolia with eruptions as recently as 5,000 years ago (Barry et al. 2003). The Chuluut region, located 100 km to the south, is one of the largest volcanic provinces in central Mongolia and has erupted lavas from 0.3–6 million years ago (Ancuta et al. 2018). Based on a geochemical analysis of the erupted lavas, (Ancuta et al. 2018) estimated samples in these regions were derived from 4% partial melting at a depth of 90 km and Harris et al. (2010) predicted fast magma ascent directly from the mantle with no crustal magma storage.

The anomalous features are spatially associated with the surface expressions of volcanism (volcanic cones and calderas) and modern-day hydrothermal activity (hot springs), suggesting a relation (Comeau et al. 2018a, see Fig. 1). Geochemical evidence is inconsistent with crustal melt storage below the Hangai Dome (e.g. Harris et al. 2010). Therefore, one potential explanation for these features may be hydrothermal alteration from ancient conduits of hot magma as it moved through the crust (e.g. Cashman & Sparks 2013), which would produce a small, but detectable, signature in the magnetotelluric data (Comeau 2015; Comeau et al. 2016).

Below these volcanic regions there is evidence that indicates partial melt generation in a shallowing asthenosphere (see Sec. 5.2.1). Therefore, the Tariat and Chuluut volcanism can be potentially traced throughout the lithospheric column, from the upper crustal anomalous zones possibly representing the signature of ancient magma conduits coincident with surface calderas, to the deep conductive zone possibly related to a shallowing asthenosphere and a source zone of partial melt. Consequently, this is a nice test of our inversion strategy that was designed to bridge multiple spatial scales.

6   CONCLUSION

In this study we present the first 3-D resistivity model of the Hangai and Gobi-Altai region in Mongolia. The final electrical resistivity model successfully resolves features across multiple spatial scales, featuring small ($<$ 3 km) crustal resistivity structures along with large-scale regional resistivity variations ($>$100 km) at the Lithosphere-Asthenosphere boundary within the same self-consistent model.

Magnetotelluric data were acquired over an area of 650×400 km^2 in the Hangai and Gobi-Altai mountains in central Mongolia. A station layout was designed that combines 97 sites on a regularly spaced 50 km grid with 175 sites along profiles and in local areas of interest that have a denser spacing of 5 to 15 km. Efficient data acquisition was achieved by the use of telluric-only instruments and deriving telluric-magnetotelluric transfer functions for the profiles. The estimated transfer functions used for the inversion covered a period range from 0.1 to 20000 s.

Numerical modelling and inversion of MT data that encompass a wide period range and a non-uniform site distribution poses a computationally challenging problem that requires an approach that can account for the inherent multiscale nature of the data. The addition of topography adds further complications. The technical aspects were addressed by using a finite-element method (FEM) inversion algorithm based on non-conforming hexahedral meshes, which facilitates multi-scale model parametrizations and allowed the incorporation of local topography while keeping computational cost feasible. Furthermore, we developed a multi-stage inversion methodology, whereby additional sites, a wider period range, and a finer model discretization was included in subsequent stages.

For Stage I, a regional 1-D resistivity model was derived to act as an initial model for Stage II, the 3-D inversion with data from the coarse grid sites. The resulting model was then passed on to Stage III, where all sites with denser spacing were added, followed by Stage IV with an extended period range and a finer mesh. This approach decreased the risk of landing in a geologically implausible local minimum of the parameter space. As a result,

we obtained a resistivity model that accurately resolves small resistivity structures in the crust together with regional resistivity variations down to the asthenosphere.

This approach can further be extended to both larger and smaller scales. For example, the use of long period instruments on a coarser grid could extend the model resolution beyond the lithosphere-asthenosphere-boundary. Alternatively, a focused inversion, limited to a small subset of the region but using a finer grid and short period transfer functions, could act as a high resolution fifth stage and facilitate local studies of mineralized (Comeau et al. 2018b) and geothermal zones (Batmagnai et al. 2019).

The final 3-D resistivity model reveals a highly resistive (2000–20000 Ωm) upper crust (0–20 km) in the Hangai region, which is consistent with a pre-Cambrian, cratonic basement. Furthermore, many conductive anomalies are imaged in the upper crust that are coincident with, and can potentially be explained by surface observables, such as faults zones, mineral zones, volcanic provinces, and geothermal areas. Thanks to the multiscale approach, some of these anomalies can be traced continuously to asthenospheric depths. In contrast to the resistive upper crust, the lower crust (30–50 km) consists of well-resolved low-resistivity zones (5–50 Ωm), some of them in tube-like shapes. A possible explanation are fluid-rich domains that are trapped within the ductile lower crust. A large low-resistivity zone (30–100 Ωm) is imaged in the upper mantle, which features features two localized upward bulges below the Hangai Dome. This result is consistent with a non-uniform lithosphere-asthenosphere boundary that contains small upwellings, shallowing to a depth of only 70 km. However, the origin of such upwellings can not be constrained with the resistivity model alone. It provides crucial structural information from the shallow crust to the upper mantle, but more research is needed to constrain the geodynamic processes, which are the cause for the upwelling and ultimately for the intraplate volcanism and the Hangai Dome uplift.

REFERENCES

Alzetta, G., Arndt, D., Bangerth, W., Boddu, V., Brands, B., Davydov, D., Gassmöller, R., Heister, T., Heltai, L., Kormann, K., et al., 2018. The deal. II library, version 9.0, *Journal of Numerical Mathematics*, **26**(4), 173–183.

Ancuta, L. D., Zeitler, P. K., Idleman, B. D., & Jordan, B. T., 2018. Whole-rock 40Ar/39Ar geochronology, geochemistry, and stratigraphy of intraplate Cenozoic volcanic rocks, central Mongolia, *Bulletin*, **130**(7-8), 1397–1408.

Aster, R. C., Borchers, B., & Thurber, C. H., 2018. *Parameter estimation and inverse problems*, Elsevier.

Badarch, G., Cunningham, W. D., & Windley, B. F., 2002. A new terrane subdivision for Mongolia: implications for the Phanerozoic crustal growth of Central Asia, *Journal of Asian Earth Sciences*, **21**(1), 87–110.

Bahr, K., 1991. Geological noise in magnetotelluric data: a classification of distortion types, *Physics of the Earth and Planetary Interiors*, **66**(1), 24 – 38.

Balay, S., Abhyankar, S., Adams, M. F., Brown, J., Brune, P., Buschelman, K., Dalcin, L., Dener, A., Eijkhout, V., Gropp, W. D., Kaushik, D., Knepley, M. G., May, D. A., McInnes, L. C., Mills, R. T., Munson, T., Rupp, K., Sanan, P., Smith, B. F., Zampini, S., Zhang, H., & Zhang, H., 2018. PETSc users manual, Tech. Rep. ANL-95/11 - Revision 3.10, Argonne National Laboratory.

Bao, X., Eaton, D. W., & Guest, B., 2014. Plateau uplift in western Canada caused by lithospheric delamination along a craton edge, *Nature Geoscience*, **7**(11), 830.

Barry, T., Saunders, A., Kempton, P., Windley, B., Pringle, M., Dorjnamjaa, D., & Saandar, S.,

2003. Petrogenesis of Cenozoic basalts from Mongolia: evidence for the role of asthenospheric versus metasomatized lithospheric mantle sources, *Journal of Petrology*, **44**(1), 55–91.

Batmagnai, E., Samrock, F., Grayver, Alexander, V., Kuvshinov, A., Saar, Martin, O., Demberel, S., Tsegmed, B., Tserendug, S., Purevsuren, D., & Oyuntsetseg, D., 2019. Integrated geoscientific exploration for geothermal energy utilization in the Mongolian Hangai, in *EGU General Assembly Conference Abstracts*, Vienna, Austria.

Berdichevsky, M., Vanyan, L., Kuznetsov, V., Levadny, V., Mandelbaum, M., Nechaeva, G., Oku-lessky, B., Shilovsky, P., & Shpak, I., 1980. Geoelectrical model of the Baikal region, *Physics of the Earth and Planetary Interiors*, **22**(1), 1 – 11.

Bertrand, E., Caldwell, T., Hill, G., Wallin, E., Bennie, S., Cozens, N., Onacha, S., Ryan, G., Walter, C., Zaino, A., et al., 2012. Magnetotelluric imaging of upper-crustal convection plumes beneath the Taupo Volcanic Zone, New Zealand, *Geophysical Research Letters*, **39**(2).

Bird, P., 1979. Continental delamination and the Colorado Plateau, *Journal of Geophysical Research: Solid Earth*, **84**(B13), 7561–7571.

Booker, J. R., 2014. The magnetotelluric phase tensor: A critical review, *Surveys in Geophysics*, **35**(1), 7–40.

Buchan, C., Cunningham, D., Windley, B. F., & Tomurhuu, D., 2001. Structural and lithological characteristics of the Bayankhongor Ophiolite Zone, Central Mongolia, *Journal of the Geological Society*, **158**(3), 445–460.

Cagniard, L., 1953. Basic theory of the magneto-telluric method of geophysical prospecting, *Geophysics*, **18**(3), 605–635.

Calais, E., Vergnolle, M., San'Kov, V., Lukhnev, A., Miroshnitchenko, A., Amarjargal, S., & Déverchère, J., 2003. GPS measurements of crustal deformation in the Baikal-Mongolia area (1994–2002): Implications for current kinematics of Asia, *Journal of Geophysical Research: Solid Earth*, **108**(B10).

Campanyà, J., Ledo, J., Queralt, P., Marcuello, A., & Jones, A. G., 2014. A new methodology to estimate magnetotelluric (MT) tensor relationships: Estimation of Local transfer-functIons by Combining Interstation Transfer-functions (ELICIT), *Geophysical Journal International*, **198**(1), 484–494.

Cashman, K. V. & Sparks, R. S. J., 2013. How volcanoes work: A 25 year perspective, *GSA bulletin*, **125**(5-6), 664–690.

Chen, M., Niu, F., Liu, Q., & Tromp, J., 2015. Mantle-driven uplift of Hangai Dome: New seismic constraints from adjoint tomography, *Geophysical Research Letters*, **42**(17), 6967–6974.

Cherevatova, M., Smirnov, M. Y., Korja, T., Pedersen, L. B., Ebbing, J., Gradmann, S., Becken, M., Group, M. W., et al., 2015. Electrical conductivity structure of north-west Fennoscandia

from three-dimensional inversion of magnetotelluric data, *Tectonophysics*, **653**, 20–32.

Comeau, M., 2015. *Electrical Resistivity Structure of the Altiplano-Puna Magma Body and Volcan Uturuncu from Magnetotelluric Data: University of Alberta*, Ph.D. thesis, PhD thesis published by The University of Alberta Education and Research Archive, 337 pp.

Comeau, M. J., Unsworth, M. J., & Cordell, D., 2016. New constraints on the magma distribution and composition beneath Volcán Uturuncu and the southern Bolivian Altiplano from magnetotelluric data, *Geosphere*, **12**(5), 1391–1421.

Comeau, M. J., Becken, M., Käufl, J., Kuvshinov, A., Demberel, S., & the Hangai Working Group, 2018a. Images of intraplate volcanism: The upper crustal structure below Tariat volcanic zone, Mongolia, imaged with magnetotellurics, in *EGU General Assembly Conference Abstracts*, Vienna, Austria.

Comeau, M. J., Käufl, J., Becken, M., Kuvshinov, A., Grayver, A., Kamm, J., Demberel, S., Batmagnai, E., Tserendug, S., Eldev-Ochir, B., & Nasan-Ochir, T., 2018b. Electrical resistivity models reveal mineralization and fault systems in the Valley of the Lakes, south-central Mongolia, in *24th EM Induction Workshop Abstracts*, Helsingør, Denmark.

Comeau, M. J., Käufl, J. S., Becken, M., Kuvshinov, A., Grayver, A. V., Kamm, J., Demberel, S., Sukhbaatar, U., & Batmagnai, E., 2018c. Evidence for fluid and melt generation in response to an asthenospheric upwelling beneath the Hangai Dome, Mongolia, *Earth and Planetary Science Letters*, **487**, 201 – 209.

Comeau, M. J., Becken, M., Grayver, A., Käufl, J., & Kuvshinov, A., 2019a. Can a conceptual mechanism of fluid focusing explain lower crustal conductors?, in *Schmucker-Weidelt Colloquium for Electromagnetic Depth Research*, Haltern am See, Germany.

Comeau, M. J., Becken, M., Käufl, J., Grayver, A., Kuvshinov, A., Tserendug, S., Batmagnai, E., & Demberel, S., 2019b. Evidence for terrane boundaries and suture zones across Southern Mongolia detected with a 2-dimensional magnetotelluric transect, *Earth, Planets and Space*, in revision.

Connolly, J. & Podladchikov, Y. Y., 2013. A hydromechanical model for lower crustal fluid flow, in *Metasomatism and the chemical transformation of rock*, pp. 599–658, Springer.

Connolly, J. A. D. & Podladchikov, Y. Y., 2004. Fluid flow in compressive tectonic settings: Implications for midcrustal seismic reflectors and downward fluid migration, *Journal of Geophysical Research: Solid Earth*, **109**(B4).

Cunningham, W., 2001. Cenozoic normal faulting and regional doming in the southern Hangay region, Central Mongolia: implications for the origin of the Baikal rift province, *Tectonophysics*, **331**(4), 389–411.

Dmitriev, V. I., Il'inskii, A. S., & Sveshnikov, A. G., 1976. The developments of mathematical

methods for the study of direct and inverse problems in electrodynamics, *Russian Mathematical Surveys*, **31**(6), 133.

Dong, H., Wei, W., Jin, S., Ye, G., Zhang, L., Jing, J., Yin, Y., Xie, C., & Jones, A. G., 2016. Extensional extrusion: Insights into south-eastward expansion of Tibetan Plateau from magnetotelluric array data, *Earth and Planetary Science Letters*, **454**, 78 – 85.

Egbert, G. D., 2002. Processing and interpretation of electromagnetic induction array data, *Surveys in geophysics*, **23**(2-3), 207–249.

Egbert, G. D. & Booker, J. R., 1986. Robust estimation of geomagnetic transfer functions, *Geophysical Journal of the Royal Astronomical Society*, **87**(1), 173–194.

Ganbat, E. & Demberel, O., 2010. Geologic background of the Hangay geothermal system, west-central Mongolia, in *Proceedings World Geothermal Congress*, p. 1e6.

García, X. & Jones, A. G., 2005. A new methodology for the acquisition and processing of audio-magnetotelluric (AMT) data in the AMT dead band, *Geophysics*, **70**(5), G119–G126.

Grayver, A. V., 2015. Parallel three-dimensional magnetotelluric inversion using adaptive finite-element method. Part I: theory and synthetic study, *Geophysical Journal International*, **202**(1), 584–603.

Grayver, A. V. & Kolev, T. V., 2015. Large-scale 3D geoelectromagnetic modeling using parallel adaptive high-order finite element method, *Geophysics*, **80**(6), E277–E291.

Grayver, A. V. & Kuvshinov, A. V., 2016. Exploring equivalence domain in nonlinear inverse problems using covariance matrix adaption evolution strategy (CMAES) and random sampling, *Geophysical Journal International*, **205**(2), 971–987.

Groom, R. W. & Bailey, R. C., 1989. Decomposition of magnetotelluric impedance tensors in the presence of local three-dimensional galvanic distortion, *Journal of Geophysical Research: Solid Earth*, **94**(B2), 1913–1925.

Guy, A., Schulmann, K., Janoušek, V., Štípská, P., Armstrong, R., Belousova, E., Dolgopolova, A., Seltmann, R., Lexa, O., Jiang, Y., et al., 2015. Geophysical and geochemical nature of relaminated arc-derived lower crust underneath oceanic domain in southern Mongolia, *Tectonics*, **34**(5), 1030–1053.

Harpering, D., 2018. *Robust processing scheme for magnetotelluric data*, Master's thesis, WWU Münster.

Harris, N., Hunt, A., Parkinson, I., Tindle, A., Yondon, M., & Hammond, S., 2010. Tectonic implications of garnet-bearing mantle xenoliths exhumed by Quaternary magmatism in the Hangay dome, central Mongolia, *Contributions to Mineralogy and Petrology*, **160**(1), 67–81.

Heise, W., Bibby, H. M., Caldwell, T. G., Bannister, S. C., Ogawa, Y., Takakura, S., & Uchida, T., 2007. Melt distribution beneath a young continental rift: the Taupo Volcanic Zone, New

Zealand, *Geophysical Research Letters*, **34**(14).

Hermance, J. F. & Thayer, R. E., 1975. The telluric-magnetotelluric method, *Geophysics*, **40**(4), 664–668.

Hill, G. J., Bibby, H. M., Ogawa, Y., Wallin, E. L., Bennie, S. L., Caldwell, T. G., Keys, H., Bertrand, E. A., & Heise, W., 2015. Structure of the Tongariro Volcanic system: Insights from magnetotelluric imaging, *Earth and Planetary Science Letters*, **432**, 115–125.

Hunt, A. C., Parkinson, I., Harris, N., Barry, T., Rogers, N., & Yondon, M., 2012. Cenozoic volcanism on the Hangai Dome, Central Mongolia: geochemical evidence for changing melt sources and implications for mechanisms of melting, *Journal of Petrology*, **53**(9), 1913–1942.

Iliceto, V. & Santarato, G., 1986. On the possibility of the telluric method: some results on faulted structures, *Geophysical prospecting*, **34**(7), 1082–1098.

Ionov, D., 2002. Mantle structure and rifting processes in the Baikal–Mongolia region: geophysical data and evidence from xenoliths in volcanic rocks, *Tectonophysics*, **351**(1-2), 41–60.

Joshi, A., Bangerth, W., & Sevick-Muraca, E. M., 2004. Adaptive finite element based tomography for fluorescence optical imaging in tissue, *Optics Express*, **12**(22), 5402–5417.

Karypis, G. & Kumar, V., 1999. A fast and highly quality multilevel scheme for partitioning irregular graphs, *Journal on Scientific Computing*, **20**(1), 359–392.

Käufl, J. S., Grayver, A. V., & Kuvshinov, A. V., 2018. Topographic distortions of magnetotelluric transfer functions: a high-resolution 3-d modelling study using real elevation data, *Geophysical Journal International*, **215**(3), 1943–1961.

Kay, R. W. & Kay, S. M., 1993. Delamination and delamination magmatism, *Tectonophysics*, **219**(1-3), 177–189.

Khoza, T. D., Jones, A. G., Muller, M. R., Evans, R. L., Miensopust, M. P., & Webb, S. J., 2013. Lithospheric structure of an Archean craton and adjacent mobile belt revealed from 2-D and 3-D inversion of magnetotelluric data: Example from southern Congo craton in northern Namibia, *Journal of Geophysical Research: Solid Earth*, **118**(8), 4378–4397.

Krystopowicz, N. J. & Currie, C. A., 2013. Crustal eclogitization and lithosphere delamination in orogens, *Earth and Planetary Science Letters*, **361**, 195–207.

Liu, L. & Hasterok, D., 2016. High-resolution lithosphere viscosity and dynamics revealed by magnetotelluric imaging, *Science*, **353**(6307), 1515–1519.

Manning, C. E., 2018. Fluids of the lower crust: deep is different, *Annual Review of Earth and Planetary Sciences*, **46**, 67–97.

McDannell, K. T., Zeitler, P. K., & Idleman, B. D., 2018. Relict topography within the Hangay Mountains in central Mongolia: Quantifying long-term exhumation and relief change in an old landscape, *Tectonics*, **37**(8), 2531–2558.

Meissner, R. & Mooney, W., 1998. Weakness of the lower continental crust: a condition for delamination, uplift, and escape, *Tectonophysics*, **296**(1-2), 47–60.

Melosh, G., Cumming, W., Benoit, D., Wilmarth, M., Colvin, A., Winick, J., Soto-Neira, E., Sussman, D., Urzúa-Monsalve, L., Powell, T., et al., 2010. Exploration results and resource conceptual model of the Tolhuaca geothermal field, Chile, in *Proceedings, World Geothermal Congress*.

Meqbel, N. M., Egbert, G. D., Wannamaker, P. E., Kelbert, A., & Schultz, A., 2014. Deep electrical resistivity structure of the northwestern US derived from 3-D inversion of USArray magnetotelluric data, *Earth and Planetary Science Letters*, **402**, 290–304.

Miensopust, M. P., 2017. Application of 3-D electromagnetic inversion in practice: Challenges, pitfalls and solution approaches, *Surveys in Geophysics*, **38**(5), 869–933.

Muñoz, G., 2014. Exploring for geothermal resources with electromagnetic methods, *Surveys in geophysics*, **35**(1), 101–122.

Murphy, B. S. & Egbert, G. D., 2017. Electrical conductivity structure of southeastern North America: implications for lithospheric architecture and Appalachian topographic rejuvenation, *Earth and Planetary Science Letters*, **462**, 66–75.

NASA JPL, 2013. NASA Shuttle Radar Topography Mission Global 1 arc second. NASA LP DAAC, https://doi.org/10.5067/MEaSUREs/SRTM/SRTMGL1.003.

Nieuwenhuis, G., Unsworth, M. J., Pana, D., Craven, J., & Bertrand, E., 2014. Three-dimensional resistivity structure of Southern Alberta, Canada: implications for Precambrian tectonics, *Geophysical Journal International*, **197**(2), 838–859.

Oyuntsetseg, D., Ganchimeg, D., Minjigmaa, A., Ueda, A., & Kusakabe, M., 2015. Isotopic and chemical studies of hot and cold springs in western part of Khangai Mountain region, Mongolia, for geothermal exploration, *Geothermics*, **53**, 488–497.

Peacock, J. R., Mangan, M. T., McPhee, D., & Wannamaker, P. E., 2016. Three-dimensional electrical resistivity model of the hydrothermal system in Long Valley Caldera, California, from magnetotellurics, *Geophysical Research Letters*, **43**(15), 7953–7962.

Petit, C., Tiberi, C., Deschamps, A., & Déverchère, J., 2008. Teleseismic traveltimes, topography and the lithospheric structure across central Mongolia, *Geophysical Research Letters*, **35**(11).

Platz, A. & Weckmann, U., 2019. An automated new pre-selection tool for noisy Magnetotelluric data using the Mahalanobis distance and magnetic field constraints, *Geophysical Journal International*.

Priestley, K., Debayle, E., McKenzie, D., & Pilidou, S., 2006. Upper mantle structure of eastern Asia from multimode surface waveform tomography, *Journal of Geophysical Research: Solid Earth*, **111**(B10).

Rikitake, T., 1948. Notes on electromagnetic induction within the Earth, *Bull. Earthq. Res. Inst*, **24**(1), 4.

Rizza, M., Ritz, J.-F., Prentice, C., Vassallo, R., Braucher, R., Larroque, C., Arzhannikova, A., Arzhannikov, S., Mahan, S., Massault, M., et al., 2015. Earthquake geology of the Bulnay fault (Mongolia), *Bulletin of the Seismological Society of America*, **105**(1), 72–93.

Robertson, K., Heinson, G., & Thiel, S., 2016. Lithospheric reworking at the Proterozoic-Phanerozoic transition of Australia imaged using AusLAMP Magnetotelluric data, *Earth and Planetary Science Letters*, **452**, 27 – 35.

Robertson, K., Heinson, G., Taylor, D., & Thiel, S., 2017. The lithospheric transition between the Delamerian and Lachlan orogens in western Victoria: new insights from 3D magnetotelluric imaging, *Australian Journal of Earth Sciences*, **64**(3), 385–399.

Rousseeuw, P. J., 1984. Least median of squares regression, *Journal of the American Statistical Association*, **79**(388), 871–880.

Rung-Arunwan, T., Siripunvaraporn, W., & Utada, H., 2016. On the Berdichevsky average, *Physics of the Earth and Planetary Interiors*, **253**, 1 – 4.

Sahagian, D., Proussevitch, A., Ancuta, L., Idleman, B., & Zeitler, P., 2016. Uplift of Central Mongolia recorded in vesicular basalts, *The Journal of Geology*, **124**(4), 435–445.

Samrock, F., Grayver, A. V., Eysteinsson, H., & Saar, M. O., 2018. Magnetotelluric image of transcrustal magmatic system beneath the Tulu Moye geothermal prospect in the Ethiopian rift, *Geophysical Research Letters*, **45**(23), 12–847.

Sheldrick, T. C., Barry, T. L., Millar, I. L., Barfod, D. N., Halton, A. M., & Smith, D. J., 2019. Evidence for southward subduction of the mongol-okhotsk oceanic plate: implications from mesozoic adakitic lavas from mongolia, *Gondwana Research*.

Smith, J. T., 1997. Estimating galvanic-distortion magnetic fields in magnetotellurics, *Geophysical Journal International*, **130**(1), 65–72.

Styron, R., 2018. GEM global active faults, http://doi.org/10.5281/zenodo.1404388.

Tiberi, C., Deschamps, A., Déverchère, J., Petit, C., Perrot, J., Appriou, D., Mordvinova, V., Dugaarma, T., Ulzibaat, M., & Artemiev, A., 2008. Asthenospheric imprints on the lithosphere in central Mongolia and southern Siberia from a joint inversion of gravity and seismology (MOBAL experiment), *Geophysical Journal International*, **175**(3), 1283–1297.

Tietze, K. & Ritter, O., 2013. Three-dimensional magnetotelluric inversion in practice-the electrical conductivity structure of the San Andreas Fault in Central California, *Geophysical Journal International*, **195**(1), 130–147.

Tikhonov, A., 1950. On determining electrical characteristics of the deep layers of the Earths crust, in *Doklady*, vol. 73, pp. 295–297, Citeseer.

Tikhonov, A. N., 1963. On the solution of ill-posed problems and the method of regularization, in *Doklady Akademii Nauk*, vol. 151, pp. 501–504, Russian Academy of Sciences.

Unsworth, M. & Bedrosian, P. A., 2004. Electrical resistivity structure at the SAFOD site from magnetotelluric exploration, *Geophysical Research Letters*, **31**(12).

Unsworth, M. & Rondenay, S., 2013. *Mapping the Distribution of Fluids in the Crust and Lithospheric Mantle Utilizing Geophysical Methods*, pp. 535–598, Springer Berlin Heidelberg, Berlin, Heidelberg.

Usui, Y., Ogawa, Y., Aizawa, K., Kanda, W., Hashimoto, T., Koyama, T., Yamaya, Y., & Kagiyama, T., 2016. Three-dimensional resistivity structure of Asama volcano revealed by data-space magnetotelluric inversion using unstructured tetrahedral elements, *Geophysical Journal International*, **208**(3), 1359–1372.

Van der Voo, R., van Hinsbergen, D. J., Domeier, M., Spakman, W., & Torsvik, T. H., 2015. Latest Jurassic–earliest Cretaceous closure of the Mongol-Okhotsk Ocean: A paleomagnetic and seismological-tomographic analysis, *Geological Society of America Special Papers*, **513**, 589–606.

Vergnolle, M., Pollitz, F., & Calais, E., 2003. Constraints on the viscosity of the continental crust and mantle from GPS measurements and postseismic deformation models in western Mongolia, *Journal of Geophysical Research: Solid Earth*, **108**(B10).

Walker, R., Nissen, E., Molor, E., & Bayasgalan, A., 2007. Reinterpretation of the active faulting in central Mongolia, *Geology*, **35**(8), 759–762.

Walker, R., Molor, E., Fox, M., & Bayasgalan, A., 2008. Active tectonics of an apparently aseismic region: distributed active strike-slip faulting in the Hangay Mountains of central Mongolia, *Geophysical Journal International*, **174**(3), 1121–1137.

Weidelt, P., 1972. The inverse problem of geomagnetic induction, *J. Geophys.*, **38**, 257–289.

Windley, B. F. & Allen, M. B., 1993. Mongolian plateau: Evidence for a late Cenozoic mantle plume under central Asia, *Geology*, **21**(4), 295–298.

Xu, S., Unsworth, M. J., Hu, X., & Mooney, W. D., 2019. Magnetotelluric evidence for asymmetric simple shear extension and lithospheric thinning in south China, *Journal of Geophysical Research: Solid Earth*, **124**(1), 104–124.

Yang, B., Egbert, G. D., Kelbert, A., & Meqbel, N. M., 2015. Three-dimensional electrical resistivity of the north-central USA from EarthScope long period magnetotelluric data, *Earth and Planetary Science Letters*, **422**, 87 – 93.

Yungul, S. H., 1977. The telluric methods in the study of sedimentary structures-a survey, *Geoexploration*, **15**(4), 207–238.

Zhang, F., Wu, Q., Grand, S. P., Li, Y., Gao, M., Demberel, S., Ulziibat, M., & Sukhbaatar, U., 2017. Seismic velocity variations beneath central Mongolia: Evidence for upper mantle plumes?,

988 *Earth and Planetary Science Letters*, **459**, 406–416.